Stepwise Solar Methane Reforming and Water-Splitting via Lattice Oxygen Transfer in Iron and Cerium Oxides

Srirat Chuayboon, Stéphane Abanades, Sylvain Rodat

Stepwise solar methane reforming and water-splitting via lattice oxygen transfer in iron and cerium oxides

Srirat Chuayboon, Stéphane Abanades[*]*, Sylvain Rodat*

Dr. S. Abanades
Processes, Materials and Solar Energy Laboratory, PROMES-CNRS, 7 Rue du Four Solaire, 66120 Font-Romeu, France
E-mail: stephane.abanades@promes.cnrs.fr

S. Chuayboon
Processes, Materials and Solar Energy Laboratory, PROMES-CNRS, 7 Rue du Four Solaire, 66120 Font-Romeu, France
Department of Mechanical Engineering, King Mongkut's Institute of Technology Ladkrabang, Prince of Chumphon Campus, Chumphon 86160, Thailand

Dr. S. Rodat
Univ. Grenoble Alpes, INES, BP 332, 50 Avenue du Lac Léman, F-73375 Le-Bourget-du-lac, France. CEA-LITEN Laboratoire des Systèmes Solaires Haute Température (LSHT), F-38054 Grenoble, France

Keywords: (concentrated solar energy, chemical looping, ceria, iron oxide, syngas)

Abstract. Chemical looping reforming of methane (CLRM) involves lattice oxygen transfer in metal oxides. This study aims to compare iron (Fe_2O_3) and cerium (CeO_2) oxides as oxygen carrier materials for isothermal solar-driven stepwise CH_4 reforming and H_2O splitting. Experiments were conducted in a directly-irradiated lab-scale solar reactor heated by concentrated sunlight in the temperature range 950-1150 °C. Using solar energy for process heat reduces the dependence on fossil energy resources and avoids CO_2 emissions, while converting solar energy into chemical fuels. The performance of the oxygen carrier materials was compared and evaluated by determining the averaged amount of oxygen transferred, methane conversion, syngas yield, and thermochemical cycling stability. As a result, iron oxide reduction with methane strongly depended on temperature and displayed relatively lower reaction rate than CeO_2. The reduced iron (Fe) was not completely re-oxidized to iron oxide (Fe_3O_4) after water-splitting step because of its low thermal stability resulting in strong

sintering and agglomeration, thereby decreasing syngas yield and eventually leading to material deactivation. In contrast, cerium oxide exhibited faster reaction rate and stable syngas yield with H_2/CO molar ratio approaching two over repeated cycles. Stable patterns in the averaged oxygen nonstoichiometry (δ=0.35-0.38), methane conversion (X_{CH_4}=46.9-60.9%), and total syngas yield (5.67-6.80 mmol/g_{CeO_2} for reduction and 2.38-2.57 mmol/g_{CeO_2} for oxidation) over twelve successive cycles for ceria reticulated foam demonstrated excellent thermal cycling stability. Thus, employing Fe_2O_3 as oxygen carrier was not suitable for solar CLRM, but iron oxide reduction with methane could be a promising option for solar metallurgy aiming at producing both metallic iron and syngas.

1. Introduction

Synthesis gas (syngas) is widely considered as one of the most important valuable chemical energy carriers as it is a key intermediate resource to produce hydrogen, ammonia, methanol, or synthetic hydrocarbon fuels. The syngas can be produced from a variety of sources, including either renewable (biomass) or fossil sources (natural gas, coal, or any hydrocarbon feedstock), by partial oxidation reactions with steam or oxygen. Methane reforming is the conventional method for producing syngas. Steam [1] and dry reforming [2–5] are two possible routes for methane reforming:

Steam reforming: $CH_4+H_2O\rightarrow 3H_2+CO$ $\Delta H^0=+206$ kJ/mol (1)

Dry reforming: $CH_4+CO_2\rightarrow 2H_2+2CO$ $\Delta H^0=+247$ kJ/mol (2)

Both reactions are highly endothermic, and the required energy to drive these reactions is generally supplied by the combustion of fossil fuels, resulting in greenhouse gas emissions, especially CO_2 responsible for climate change and global warming. Using solar energy in

place of fossil fuels for supplying process heat thus represents a suitable option to alleviate these issues.

Alternatively, a promising modern pathway to produce clean syngas is the utilization of metal oxide redox pairs for partial oxidation of methane (namely, chemical looping reforming of methane, CLRM) using concentrated solar energy to drive endothermic reactions.[6–9] Such a process usually encompasses two steps: (1) partial oxidation of methane along with metal oxide reduction, and (2) re-oxidation of the oxide with steam (or CO_2) to produce pure H_2 (or CO). The advantages of solar CLRM over metal oxides when compared to the conventional process are: (1) the discharge of pollutants is totally avoided, as the required heat is provided by solar energy [10–13], (2) the use of catalysts is bypassed, eliminating deactivation issues, (3) the supply of gaseous oxygen associated with the need for upstream air separation for oxygen production are eliminated, (4) isothermal cycle operation is made possible (~1000°C), avoiding sensible heat losses and reactor materials issues [14], (5) syngas is produced with H_2/CO ratio of two, suitable for methanol synthesis, and (6) carbon deposition on redox materials is inherently eliminated during oxidation step (carbon gasification with H_2O or CO_2), thus avoiding oxygen carriers deactivation.

The possibility of utilizing metal oxides as oxygen carriers for CH_4 partial oxidation has been experimentally reported. The materials include either volatile metal oxides such as ZnO[10,15] and MgO[16], or non-volatile oxides such as WO_3[12], ceria (CeO_2)[17,18], cerium-based oxides[19–24], and iron oxide[25–27]. Cerium and iron oxides are particularly attractive because of their different physical and chemical properties.[28] Ceria keeps a stable cubic fluorite structure during large changes in oxygen non-stoichiometries (reduction extents), and exhibits rapid oxygen storage/release through lattice transfer.[29–32] On the other hand, iron oxide (Fe_2O_3) is abundant and low cost, and exhibits large oxygen releasing ability compared to CeO_2 and other candidates, but it may encounter sintering issues, leading to low cycling stability.[33,34] The main motivation of using iron oxide for CLRM is thus related to process

cost reduction because of large material availability, compared to cerium oxide. Moreover, the sintering issue of iron oxide may be counterbalanced by its superior fuel production capability due to reactions involving multivalent iron species (Fe, FeO, Fe_3O_4), thus potentially leading to higher amounts of oxygen transferred during redox reactions. Conversely, the exchanged oxygen and fuel productivity from ceria are determined by the reduction extent corresponding to the achieved non-stoichiometry (amount of oxygen vacancies in $CeO_{2-\delta}$, which is always lower than δ_{max}=0.5 mol_O/mol_{CeO_2}). Thus, evaluation and comparison of the materials reactivity for fuel production upon cycling under real solar irradiation conditions is necessary to identify the most suitable one.

Otsuka et al. first investigated the partial oxidation of CH_4 over ceria in a fixed bed quartz tubular reactor (non-solar).[18] They showed that the use of ceria enables the direct conversion of CH_4 into syngas, and the reaction provides an appropriate syngas composition (H_2/CO=2). Besides, the ceria redox cycle was coupled with the utilization of concentrated solar energy for producing H_2 from two-step thermochemical water-splitting, as first proposed by Abanades and Flamant.[35] Thermodynamic and experimental analysis of solar-driven methane reforming over ceria were also investigated.[6,30,36] Maximum predicted solar-to-fuel efficiency of 40% was reported for partial oxidation of methane with ceria during isothermal cycling at 950 °C[37], and the maximum projected solar-to-fuel thermal efficiency of 27% for cycling at 1000 °C was later identified[8]. Solar CLRM in a prototype reactor operated in a high-flux solar simulator was performed with solar-to-fuel efficiency of 7% and thermal efficiency of 25%.[9] Concerning iron oxides, Steinfeld et al. examined the Fe_3O_4+4CH_4 system and reported that the chemical equilibrium species consist of metallic iron in the solid phase and a mixture of 67% H_2 and 33% CO in the gaseous phase (at 1 bar and 1027 °C), while showing experimentally that the reduction of Fe_3O_4 with CH_4 is strongly dependent on temperature and residence time.[27] Lu et al. investigated the reactivity of magnetite (Fe_3O_4) with respect to CH_4 reforming and H_2O splitting in a continuous prototype.[33] The reduction

kinetics was also studied with both fresh and recycled magnetite. The hydrogen yields from the original and calcinated magnetite after successive cycling were 4.94 and 5.25 mmol/g, respectively, and the activation energy for the reduction was 93 kJ/mol. In addition, Bleeker et al. studied the deactivation of iron oxide used in the steam-iron process to produce hydrogen and reported that the main drawback of using iron oxide is the inherent structural changes that take place during oxygen loading and unloading, leading to severe deactivation due to loss of specific surface area.[34]

The performance comparison of the oxygen carrier materials in a solar reactor using representative operating conditions has not been performed so far. In the present work, the CLRM process is performed in a directly-irradiated lab-scale solar reactor using iron and cerium oxides with different structures (packed-bed powder and reticulated porous foam). High-temperature concentrated solar heat is used to provide the reaction enthalpy, and therefore the feedstock is entirely dedicated to produce H_2 and CO (syngas). Solar energy is thus stored into a high-quality syngas and can easily be transported for later use as a convertible and dispatchable chemical form. Solar CLRM promotes methane valorization and offers an efficient means of storing intermittent solar energy into renewable solar fuels. The relevant performance metrics of the process are quantified including lattice oxygen transfer (n_O) and average oxygen non-stoichiometry (δ), methane conversion (X_{CH_4}), syngas yield, and thermochemical cycling stability in order to compare the influence of oxygen carrier materials on solar reactor performance. In addition, the demonstration of the whole two-step solar process in a solar reactor operated with a real solar concentrating system is presented with determination of the fuel production capacity during both steps.

2. Thermodynamics

2.1. Iron oxide

The endothermic reduction reaction of iron oxide (Fe_2O_3) with CH_4 is composed of successive steps:

$$Fe_2O_3+1/3CH_4 \longrightarrow 2/3Fe_3O_4+2/3H_2+1/3CO \quad (3)$$

$$2/3Fe_3O_4+2/3CH_4 \longrightarrow 2FeO+4/3H_2+2/3CO \quad (4)$$

$$2FeO+2CH_4 \longrightarrow 2Fe+4H_2+2CO \quad (5)$$

The summation of the above reactions corresponds to:

$$Fe_2O_3+3CH_4 \rightarrow 2Fe+6H_2+3CO \qquad \Delta H^0 = 715 \text{ kJ/mol} \quad (6)$$

Possible side reactions related to methane cracking and direct reaction of Fe_2O_3 with carbon may also occur during iron oxide reduction with methane:

$$CH_4 \longrightarrow C+2H_2 \quad (7)$$

$$Fe_2O_3+3C \rightarrow 2Fe+3CO \quad (8)$$

The exothermic oxidation reaction of metallic iron with H_2O is represented as (Fe_3O_4 re-oxidation to Fe_2O_3 with H_2O is not thermodynamically possible):

$$3Fe+4H_2O \longrightarrow Fe_3O_4+4H_2 \qquad \Delta H^0 = -151 \text{ kJ/mol} \quad (9)$$

Possible side reactions during oxidation step are carbon deposition gasification with H_2O:

$$C+H_2O \longrightarrow CO+H_2 \quad (10)$$

$C+2H_2O \longrightarrow CO_2+2H_2$ (11)

The thermodynamic feasibility of chemical reactions involving iron oxide species reduction with methane can be assessed from the Gibbs free enthalpy change (ΔG°) (**Figure 1**). The ΔG° values decrease with temperature (ΔG° equals zero at 400 °C for $3Fe_2O_3+CH_4$, and at above 600 °C for the other reactions), which means that all the reduction reactions are thermodynamically favorable when increasing the temperature.

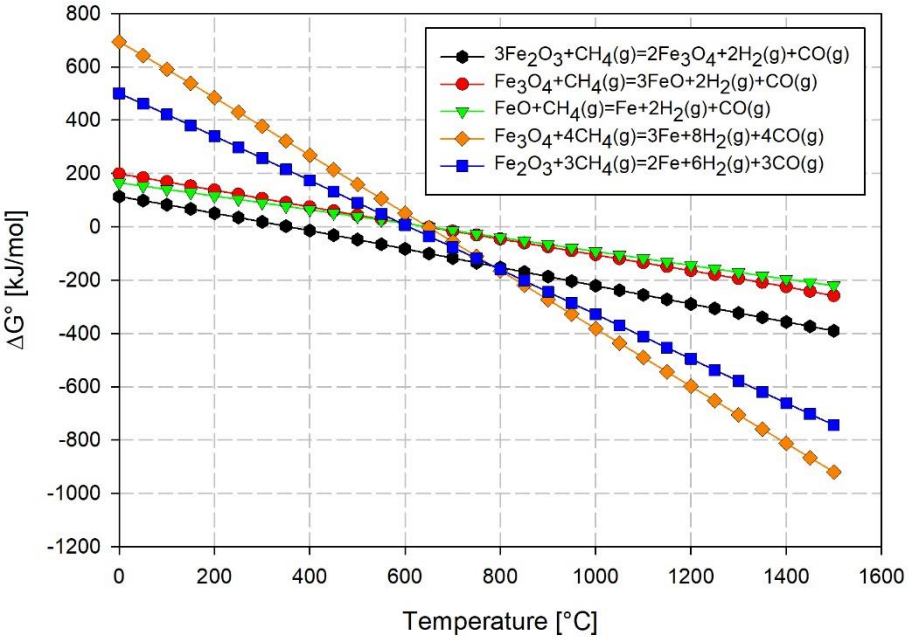

Figure 1. ΔG° variations for iron oxides reduction with methane as a function of temperature.

Regarding the possible side reactions (**Figure 2**), the direct reductions of Fe_3O_4 with C and H_2 are thermodynamically favorable (Fe_3O_4+2C and Fe_3O_4+4C proceed spontaneously at above 700 °C, and $Fe_3O_4+4H_2$ proceeds at above 1100 °C). In contrast, the direct reduction of Fe_3O_4 with CO is not thermodynamically possible.

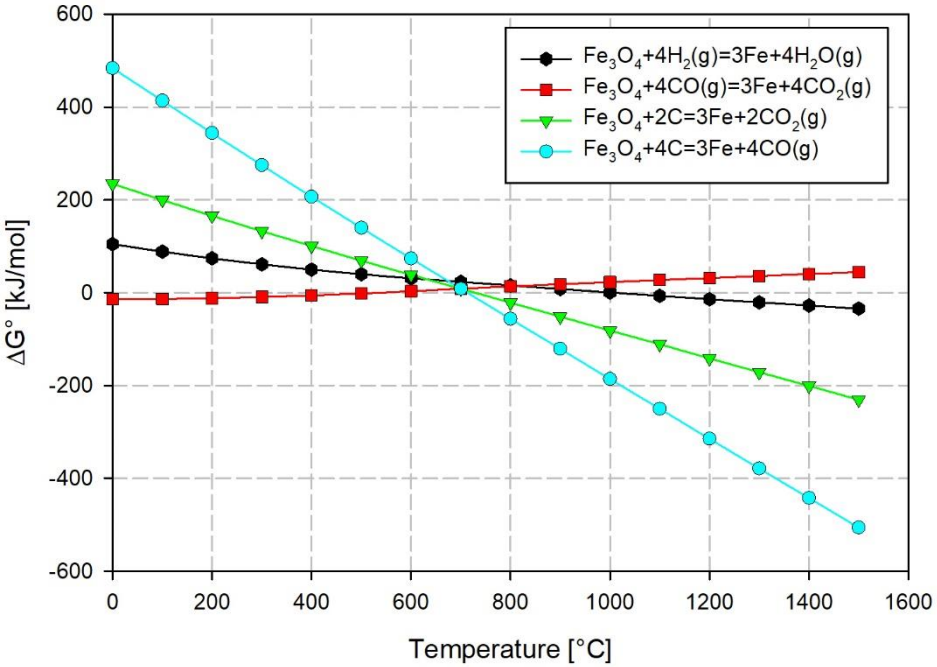

Figure 2. ΔG° variations for the reactions of Fe_3O_4 with H_2, CO, and C as a function of temperature.

The thermodynamic equilibrium composition was calculated with HSC Chemistry to appraise the species distribution and system composition as a function of temperature. It provides a realistic overview of the chemical product species and the most favorable conditions for carrying out the reduction reaction with CH_4 and reaching completion. The main assumptions of the method must be reminded, including closed system approach without any gas flow and available thermodynamic properties for any chemical species to represent the system as closely as possible.

The equilibrium species composition of Fe_2O_3+3CH_4 at 1 bar as a function of temperature is shown in **Figure 3** (and in **Figure S1** for Fe_3O_4+4CH_4). Fe_2O_3 is first reduced to Fe_3O_4 while methane is decomposed to C and H_2 when the temperature exceeds 400 °C. Then, Fe_3O_4 is reduced to FeO, along with intermediate non-stoichiometric species ($Fe_{0.945}O$, $Fe_{0.947}O$, and $FeO_{1.056}$) while H_2, C, and H_2O(g) become the main product components. Above 400 °C, FeO

starts reducing into Fe, along with CO and CO_2 formation. Complete reduction to Fe is reached above 700 °C, while C, H_2O, and CO_2 decrease constantly. Finally, the main products are both H_2 and CO with H_2/CO ratio approaching two, and Fe above 1000 °C.

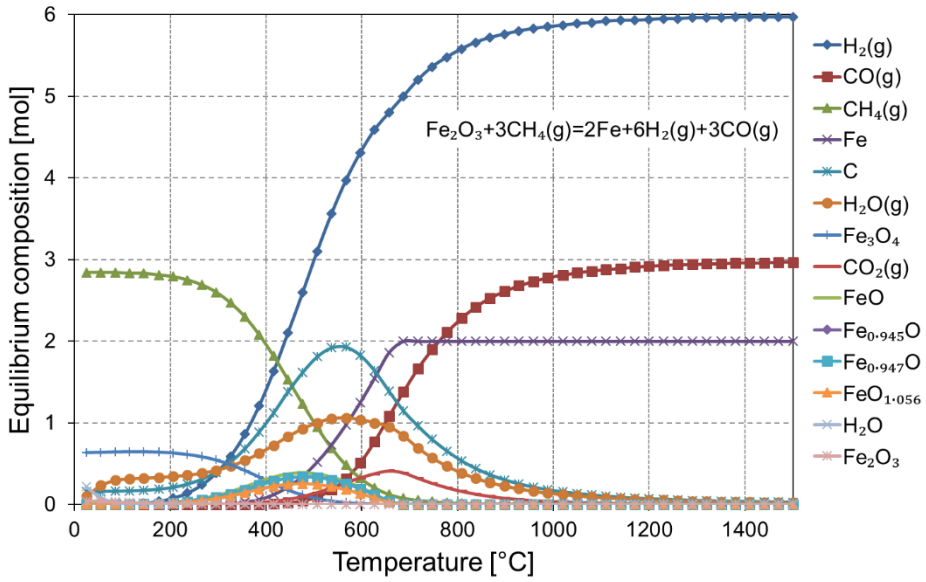

Figure 3. Thermodynamic equilibrium composition of methane reforming over Fe_2O_3 as a function of temperature at 1 bar.

Regarding carbothermal reduction of Fe_2O_3 in **Figure 4** (and **Figure S2** for Fe_3O_4+4C), Fe_2O_3 is first reduced to Fe_3O_4 along with the formation of CO_2 above 200 °C. Subsequently, Fe_3O_4 is reduced to FeO and non-stoichiometric compounds ($Fe_{0.945}O$, $Fe_{0.947}O$, and $FeO_{1.056}$) above 400 °C, and FeO is finally reduced to Fe along with CO formation above 500 °C. Reduction to Fe reaches completion at above 800 °C, while CO_2 declines continuously. The global reaction approaches completion at above 1000 °C, yielding Fe and CO.

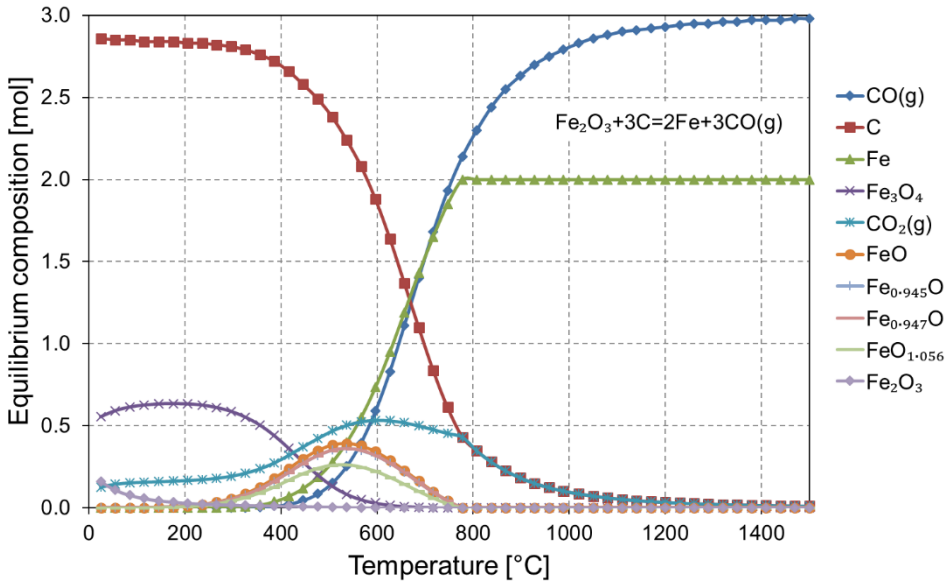

Figure 4. Thermodynamic equilibrium composition of Fe_2O_3 carbothermal reduction as a function of temperature at 1 bar.

2.2. Cerium oxide

Solar CLRM based on non-stoichiometric cerium oxide is represented as:

Reduction step: $CeO_2 + \delta CH_4 \longrightarrow CeO_{2-\delta} + \delta CO + 2\delta H_2$ (12)

Oxidation step: $CeO_{2-\delta} + \delta H_2O \longrightarrow CeO_2 + \delta H_2$ (13)

The thermodynamic equilibrium composition for the reduction step (**Figure 5**) shows that CH_4 first starts thermally decomposing into both solid carbon and H_2(g), while the reduction of CeO_2 proceeds with the formation of $CeO_{1.81}$ and $CeO_{1.78}$. Meanwhile, small amounts of both H_2O(g) and CO_2(g) are formed at the beginning of reaction. Subsequently, C deposition starts reacting with oxygen released from ceria resulting in CO formation at above 500 °C. Non-stoichiometric compounds ($CeO_{1.72}$ and $CeO_{1.83}$ mainly, and $CeO_{1.67}$ in negligible amount) are formed as intermediate species, which provide a good representation of the overall reduction mechanism during Ce(IV) reduction into Ce(III) species. The reaction

reaches completion at above 1000 °C, yielding Ce_2O_3 and H_2/CO mixture (with H_2/CO ratio approaching two).

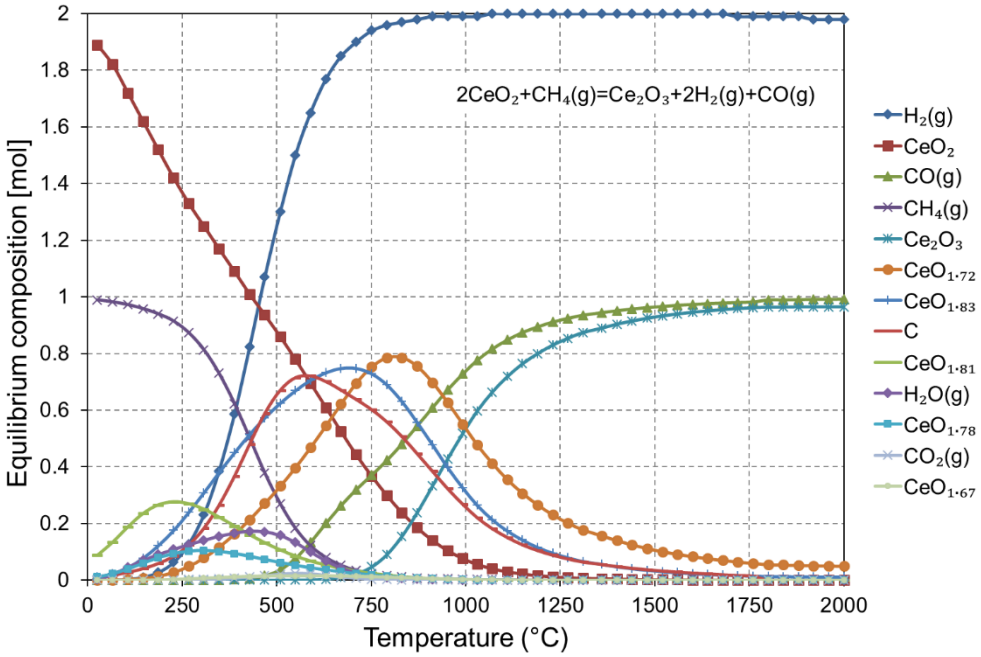

Figure 5. Thermodynamic equilibrium composition of methane reforming over ceria as a function of temperature at 1 bar.

3. Experimental set up and methods

The solar reactor concept is schematically showed in **Figure 6**.[7] The solar reactor consists of a cylindrical metallic cavity receiver with a conical part (60° angle) at its bottom (volume: 0.299 L and total height: 115 mm), wrapped by a 30 mm-thick alumino-silicate insulation layer. The insulated cavity receiver is vertically placed in a water-cooled cylindrical stainless-steel shell and then closed by an alumina cap with a 20 mm-diameter aperture for the access of concentrated sunlight. A protective graphite plate (2 mm-thick) with a 15 mm-diameter aperture is positioned on top of the alumina cap to protect it. A hemispherical transparent glass window equipped with a small fluorine window is lastly attached to the front flange edge of the reactor shell. A 2-m diameter parabolic mirror with a solar concentration ratio above 10000 suns (peak flux density of ~10.5 MW/m^2 at the focal plane for a DNI of 1

kW/m^2) is employed to concentrate sunlight to the focal point where the reactor aperture is positioned.

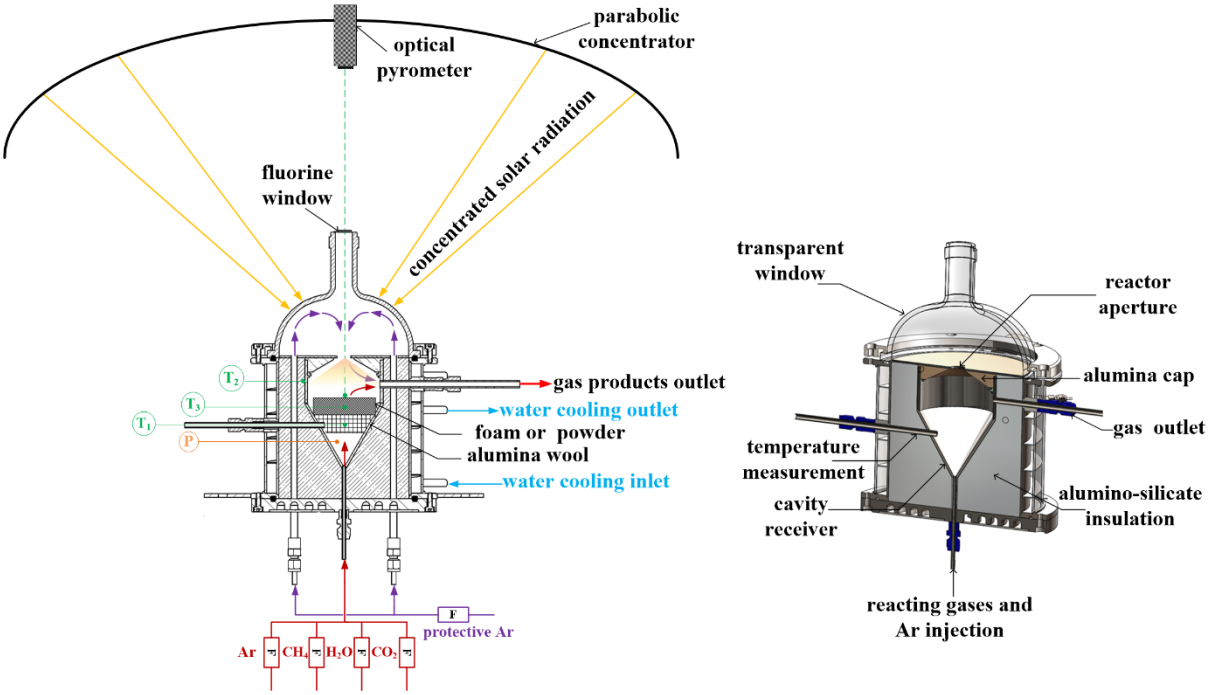

Figure 6. Schematic of the 1.5 kW_{th} directly-irradiated solar reactor and external components (left) and 3D cross section of the solar reactor (right).

Three temperatures are measured by B-type thermocouples inside the alumina wool supporting the reactive material (T_1), at the external cavity wall surface (T_2), and in the middle of samples (T_3); and an optical pyrometer (operating at 4.8-5.2 µm in a H_2O absorption band) also measures the temperature at the uppermost sample surface ($T_{pyrometer}$) through the fluorine window. In addition, the operating pressure (P) inside the cavity receiver is measured by a pressure transducer. CH_4 and Ar (gases purity of 99.999%) flow-rates are controlled by electronic Mass Flow Controllers (MFC, Brooks Instruments model SLA5850S, range 0-5 Nl/min ±0.2% of full scale), while liquid water (H_2O) flow-rate is also regulated by a MFC (range 0-30 g/h ±1% of full scale).

A given amount of cerium or iron oxide is loaded within the cavity receiver directly subjected to concentrated sunlight. The materials preparation is described in Supporting Information (materials synthesis). Two types of materials structures for each oxide (powders and porous foams) were assessed to compare their thermochemical reactivity. Since the objective is to conduct the thermochemical reactions in a solar reactor, efficient solar radiation absorption and high heat and mass transfer rates are necessary to warrant homogeneous material heating and reaction in the whole structure for utilization of the entire reactant mass. Therefore, using reticulated porous foam may be an attractive option for volumetric solar radiative absorption while offering a large available interface for gas species access and solid/gas reactions. Reactive gases (CH_4 or H_2O) and Ar carrier gas are fed via the single inlet port at the bottom of the cavity receiver. Prior to gas analysis, product gases flow through a gas scrubber composed of both bubbler and gas filtering unit (two micro filters with 0.1 µm pore diameter) to remove moisture and entrained solid carbon particles. The gas composition is then analyzed by an on-line syngas analyzer (GEIT 3100, uncertainty <±0.1% of full scale), and all the measured data are recorded by an automated data acquisition system (BECKHOFF).

The reactor cavity was initially flushed by Ar and sucked by a venturi pump to eliminate residual air from the system. Ar protective gas (2.0 Nl/min) was also provided to the window area to prevent the hot gas contact with the transparent window. Subsequently, the reactor was gradually heated by concentrated sunlight to the desired temperature (referred by T_3) under Ar. The solar power input was regulated by means of shutter opening to stabilize T_3. Once T_3 was at steady-state, a CH_4/Ar gas mixture (50% CH_4 concentration) was delivered to the reaction zone to drive the reduction reaction. After finishing reduction, reflected by H_2 and CO concentrations approaching zero, CH_4 flow was stopped and only Ar flow was fed to remove residual CH_4. Subsequently, the oxidation was performed by injecting H_2O at the same temperature (isothermal operation). The H_2O flow was stopped when H_2 evolution ceased.

The pressure was maintained at ~0.9 bar (P_{atm}= ~0.85 bar at site elevation 1,500 m above sea level) for both steps.

During partial oxidation of methane with metal oxides, the formation of both H_2O and CO_2 is also possible according to Equation 14:

$$4M_xO_y+\delta CH_4 \longrightarrow 4M_xO_{y-\delta} +\delta CO_2+2\delta H_2O \quad (14)$$

Therefore, oxygen released from the oxide structure is recovered in the forms of CO, CO_2, and H_2O (twice the amount of CO_2). The global amount of oxygen released from the oxide structure ($n_{O,red}$) is therefore determined by:

$$n_{O,red} = n_{CO} + 2n_{CO_2} + n_{H_2O} \quad (15)$$

Where n_i are the mole amounts of species i.

The replenished amount of oxygen ($n_{O,ox}$) during oxidation with H_2O (Equation 9 and 13) can be calculated from oxygen mass balance (equal to total amount of produced H_2 minus amounts produced from carbon gasification with H_2O according to Equation 10 and 11):

$$n_{O,ox} = n_{H_2} - n_{CO} - 2n_{CO_2} \quad (16)$$

Contrary to iron oxide (Fe_3O_4 cannot be reversibly oxidized with H_2O to Fe_2O_3), the partially-reduced ceria ($CeO_{2-\delta}$) can be completely re-oxidized to CeO_2. The oxygen non-stoichiometry during reduction (δ_{red}) can be defined by:

$$\delta_{red} = \frac{n_{O,red}}{n_{CeO_2}} \quad (17)$$

The replenished oxygen (δ_{ox}) during ceria oxidation with H_2O (Equation 13) can be calculated as follows:

$$\delta_{ox} = \frac{n_{O,ox}}{n_{CeO_2}} \quad (18)$$

For reduction, the CH_4 conversion is defined by:

$$X_{CH_4} = 1 - \frac{\dot{m}_{unreacted\ CH_4}}{\dot{m}_{CH_4}} \quad (19)$$

Where $\dot{m}_{unreacted\ CH_4}$ is the mass flow rate of unreacted CH_4, and $\dot{m}_{CH_4}$ is the mass flow rate of injected CH_4.

Moreover, the quality of products is assessed from the selectivity of H_2 (S_{H2}) and CO (S_{CO}) towards syngas products:

$$S_{H_2} = \frac{n_{H_2}}{n_{H_2}+n_{H_2O}} \quad (20)$$

$$S_{CO} = \frac{n_{CO}}{n_{CO}+n_{CO_2}} \quad (21)$$

Where n_{H_2} and n_{CO} are the total moles of produced H_2 and CO during oxidation and reduction steps, n_{H_2O} and n_{CO_2} the moles of produced H_2O (equal to twice the mole of CO_2) and CO_2 during reduction step.

All the operating conditions and experimental results for 29 cycles performed isothermally with iron and cerium oxides in the solar reactor are listed in Supporting Information (Table S1).

4. Results and discussion

4.1. Methane reforming over iron oxide

Pure raw Fe_2O_3 powder (total mass: 20.52 g) (**Figure S3a**) was employed as an oxygen carrier material for the solar CLRM test. Experiments were conducted with 4 cycles at 950-1100 °C. Both CH_4 and Ar carrier gas flow-rates were injected at 0.2 Nl/min for reduction step (50% inlet CH_4 mole fraction), while H_2O flow-rate was fed at 200 mg/min along with Ar carrier gas (0.2 Nl/min) for subsequent oxidation step, yielding 55% steam mole fraction at inlet.

The transient syngas production rates along with nominal reactor temperature (T_3) during iron oxide powder reduction with methane and during reduced iron oxidation with H_2O for four consecutive cycles are plotted for the respective temperatures of 1000, 1100, 950, and 1000 °C (**Figure S4**). Note that the outlet flow rate of each gas specie (F_i) was calculated from their measured mole fraction (y_i) and the known total inlet flow rate of Ar (F_{Ar}): ($F_i = F_{Ar} \cdot y_i / y_{Ar}$). During reduction step, the maximum CO_2 production rate (0.09 Nl/min) was noticed at the initial stage of the reaction at cycle #1 (Figure S4a); moreover, its amount was higher than those of CO and H_2. Actually, H_2O was also formed simultaneously in accordance with thermodynamic analysis; however, it cannot be detected from gas analysis. The CO_2 production rate was observed again at cycle #2 (but it was lower than cycle #1) when increasing the temperature to 1100 °C (Figure S4c), and after initial stage its trend remained stable along with H_2 and CO production rates. The peak H_2 and CO production rates (0.07 and 0.04 Nl/min) were found at the highest reduction temperature (1100 °C, Figure S4c). After cycle #2, the syngas (H_2, CO, and CO_2) production rates during reduction were found in negligible amounts (Figure S4e and S4g). During oxidation step, the peak of H_2 production rate (0.077 Nl/min) was also found at the same temperature (1100 °C, Figure S4d), followed by 1000 °C (0.052 Nl/min, Figure S4b) and 950 °C (0.035 Nl/min, Figure S4f), while extremely small evolution of CO and CO_2 was noticed for any oxidation temperatures. Thus, the negligible impact of carbon deposition from methane cracking was demonstrated for the CLRM over iron oxide. Noticeably, the methane reforming over iron oxide required long

duration to reach completion (because of strong oxide sintering during reduction and low available specific surface area) and strongly depended on the reduction temperature as evidenced in Figure S4c (the required reduction temperature was higher than for CH_4 reforming over ceria (see next section)). First, the reduction of fresh Fe_2O_3 to Fe_3O_4 in cycle #1 resulted in a large amount of oxygen released ($n_{O,red}$=0.095 vs. $n_{O,ox}$=0.012, **Figure 7**) in the form of CO_2. Then, during the oxidation step of cycle #1, re-oxidation to Fe_2O_3 is not possible (only Fe_3O_4 can be formed, Equation 9)[38], as evidenced by $n_{O,ox}$ much lower than $n_{O,red}$ (Figure 7). The material was deactivated after cycle #2 because operation at 1100 °C resulted in strong sintering despite achieving high reduction rate, as reflected by increased CO and H_2 production rates and maximum X_{CH_4} (33.8%).

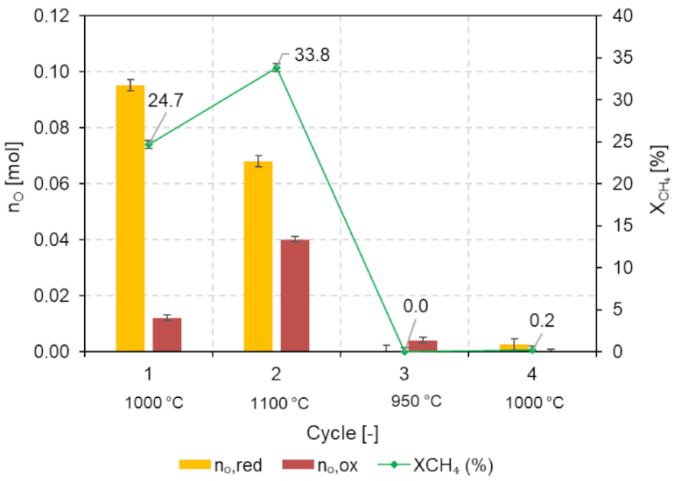

Figure 7. Comparison of $n_{O,red}$ and $n_{O,ox}$ along with CH_4 conversion during four consecutive redox cycles with iron oxide powder performed at 950-1100 °C.

Figure 8 shows the syngas yields quantified from the integration of the measured syngas production rates (Figure S4) during reduction and oxidation steps. As expected, the highest CO_2 yield (1.06 mmol/$g_{Fe_2O_3}$) was found in cycle #1, followed by cycle #2 (0.5 mmol/ $g_{Fe_2O_3}$) while the maximum total syngas yield (4.0 mmol/$g_{Fe_2O_3}$) was produced in cycle #2 (Figure. 8a), and no effect of CH_4 cracking reaction (Equation 7) was observed as evidenced by a zero

amount of H_2 (CH_4 cracking). Note that the amount of H_2 (CH_4 cracking) was quantified by the total H_2 yield measured by gas analysis minus the H_2 yield produced by the main reaction of iron oxide with methane (Equation 6), which is equivalent to twice the quantity of produced CO. In addition, no syngas production was observed in cycle #3 (the reduction reaction was negligible as evidenced by X_{CH_4}=0%, Figure 7), and a negligible syngas yield was found in cycle #4. These are because of a dramatic decrease in available surface area resulting from high sintering/coarsening and densification of the new-formed metallic iron particles after being reduced at high temperature (1100 °C, cycle #2), thereby leading to material deactivation and negligible re-oxidation. For these reasons, its powder structure cannot be backed to the initial stage despite passing re-oxidation step, thus adversely influencing the CLRM process in cycles #3 and #4 and thereby leading to negligible amounts of syngas produced. This was confirmed by the high sintering of iron powder structure observed after 4 cycles (**Figure S5**).

Figure 8b shows that most of the produced syngas yields during oxidation step was enticing from H_2 associated with the main reaction (Equation 9), and the maximum total syngas yield (2.15 mmol/$g_{Fe_2O_3}$) was found in cycle #2 in accordance with high syngas production rate in the reduction step. Moreover, negligible CO ($C+H_2O$), CO_2 ($C+2H_2O$), H_2 ($C+H_2O$), and H_2 ($C+2H_2O$) yields formed by side reactions (Equation 10 and 11) were noticed, confirming that methane cracking reaction over iron oxide is not favored at 950-1100 °C (note that the H_2 ($C+H_2O$) yield is equal to the CO yield measured by gas analysis (Equation 10), while the H_2 ($C+2H_2O$) yield is equal to twice the CO_2 yield measured by gas analysis (Equation 11)). In addition, the H_2 (Equation 20) and CO (Equation 21) selectivity (Table S1) rose sharply during cycling (e.g. from 28.6 and 34.8% at cycle #1 to 59.2 and 96.6% at cycle #3, respectively), because of the drop of H_2O and CO_2 yields. The reduced iron oxide after reduction step in cycle #4 was not re-oxidized, as it was kept for X-ray diffraction (XRD) analysis to characterize its phase composition (**Figure S6**). Phase identification shows the

presence of mainly FeO, followed by traces of Fe_3O_4 and Fe. Thus, most of the iron oxide powder did not completely reduce to Fe despite already passing the reduction step with methane, thereby confirming material deactivation.

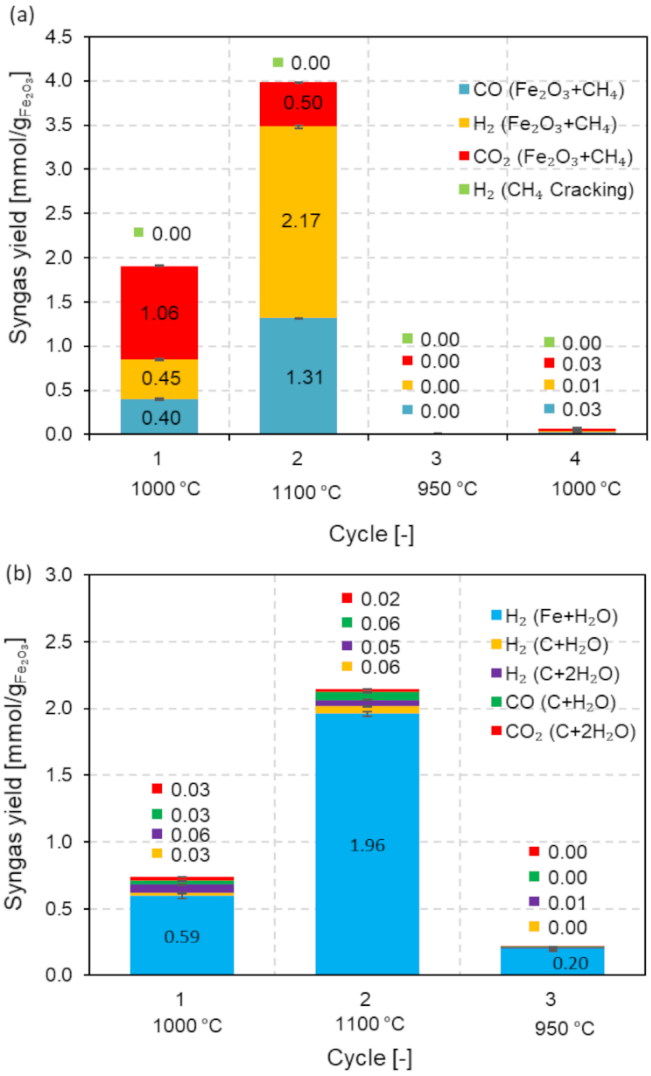

Figure 8. Syngas yields for (a) iron oxide powder reduction with CH_4 and (b) oxidation with H_2O during isothermal cycles at temperatures in the range 950-1100 °C.

In order to confirm experimental repeatability and compare the results, another iron oxide structure (reticulated porous foam, total Fe_2O_3 mass: 13.91 g) was prepared (Figure S3b) via a replication technique[7] and subsequently employed as an oxygen carrier material for the solar-driven CLRM. Experiments were conducted with seven consecutive cycles at different reduction temperatures in the range 1000-1150 °C, while the flow rates of CH_4, H_2O, and Ar

were the same as the previous tests with iron oxide powder (CH_4: 0.2 Nl/min, H_2O: 200 mg/min, and total Ar: 2.2 Nl/min).

During reduction step, the peak rates of CO_2 production decreased, while the peak of H_2 and CO remained stable with cycles repetition from cycle #1 to cycle #3 at 1000 °C (**Figure S7**). For example, the peak rates of CO_2, H_2, and CO production are 0.11, 0.02, and 0.02 Nl/min at cycle #1 compared to 0.01, 0.02, and 0.02 Nl/min at cycle #3. During oxidation step, the peak rate of H_2 production seemed to decrease slightly (0.07 Nl/min at cycle #1 compared to 0.06 Nl/min at cycle #3) while no CO and CO_2 production was evidenced. X_{CH_4} decreased dramatically from 24.9% at cycle #1 to 3.7% at cycle #3 (**Figure 9**) arising from the sharp decline in oxygen release during reduction steps of cycles #2 ($n_{O,red}$=0.012) and #3 ($n_{O,red}$=0.009) compared to cycle #1 ($n_{O,red}$=0.059), caused by non-reversible Fe_2O_3 reduction to Fe_3O_4, in agreement with thermodynamic analysis (Figure 3).

Similar to previous tests with iron oxide powder, the kinetics of methane reforming with iron oxide porous foam were too slow at 1000 °C to allow reaching completion (CH_4 injection was therefore stopped before H_2 and CO approached zero (cycles #1-3, Figure S7a, S7c and S7e)). The reaction rates were enhanced when increasing the temperature to 1050 °C according to Figure S7g and S7h. For example, the peak rates of H_2 and CO production were 0.09 and 0.05 Nl/min during reduction step (Figure S7g), while the peak rate of H_2 production was 0.11 Nl/min during oxidation step at 1050 °C, and negligible CO and CO_2 production rates were observed (Figure S7h), confirming the absence of carbon formation during reduction step. The temperature was increased to 1150 °C in cycle #5 (Figures S7i and S7j) to further hasten the kinetic rate of reduction. As a result, the syngas evolution profile (Figure S7i) increased considerably; however, the effect of methane cracking reaction was detected as reflected by the peak of H_2 after 18 min with the maximum X_{CH_4} (68.3%, Figure 9) while CO approached zero (thus indicating the end of iron oxide reduction). Note that the formed carbon can also act as reducing agent (Fe_3O_4 reduction) according to thermodynamics (Figure 4 and S2), and

the cracking reaction may also be catalyzed by the newly formed metallic iron.[27] During oxidation with H_2O, both a sharp growth in CO (consistent with the H_2 evolution profile) and a significant increase in CO_2 were noticed (Figure S7j), arising from the reaction of deposited C with H_2O and confirming that 1150 °C is favorable for CH_4 cracking reaction in this cycle. When the rate of oxide reduction is lower than the rate of methane decomposition, chemisorbed carbon may accumulate at the surface. This occurs when the rate of bulk lattice oxygen diffusion to the surface becomes lower than the CH_4 supply rate. In other words, when a lack of oxygen at the surface occurs, carbon deposition is fastened, which is increasingly favored as oxygen is being depleted during the iron oxide reduction progress.

The temperature was then decreased by 50 °C in cycle #6 to alleviate the adverse impact of CH_4 cracking reaction; nevertheless, the resulting syngas associated with CH_4 decomposition remained high as reflected by a stable H_2 evolution profile in the reduction step even if CO approached zero (Figure S7k) and a steep increase of the CO along with H_2 in the oxidation step (Figure S7l). This may possibly be also due to the carbon accumulation from the previous cycle.

The cycling experiment was completed with the reduction step performed at 1000 °C (cycle #7, Figure S7m). It was found that no CO_2 production was evolved; in contrast, the peak H_2 production rate was higher (0.06 Nl/min) while the peak CO production rate remained the same (0.02 Nl/min) as compared to those obtained from cycles #1-3. This suggests that the amount of excess available oxygen at the iron oxide surface was restrained in this last cycle, explaining the preferential formation of CO rather than CO_2 (and H_2O). Indeed, CO_2 and H_2O formation is favored when an excess amount of surface oxygen is available, thus occurring during the first cycle because the pristine oxide is Fe_2O_3. In the subsequent cycles, the participating oxide during reduction is either FeO or Fe_3O_4 (because re-oxidation to Fe_2O_3 is not thermodynamically possible when using H_2O as oxidant) with less available oxygen for

the reduction step. Moreover, selectivity increased from 23.2% to 99.7% (H_2) and 33.5% to 99.9% (CO), in agreement with the decline in CO_2 and H_2O formation during cycling.

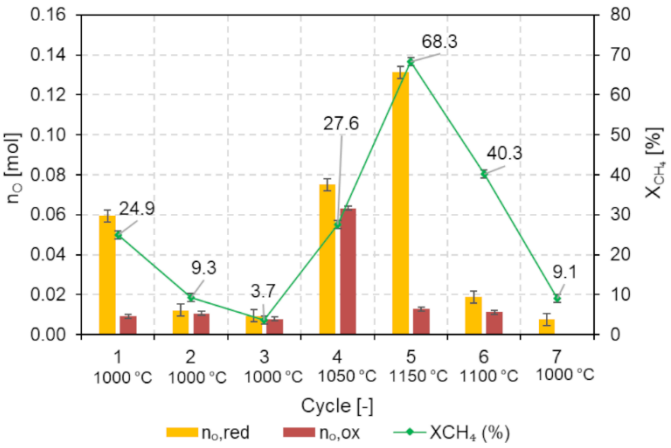

Figure 9. Comparison of $n_{O,red}$ and $n_{O,ox}$ along with CH_4 conversion during seven consecutive redox cycles with iron oxide foam performed at 1000-1150 °C.

Once again, the time integration of the measured syngas production rates in Figure S7 during reduction and oxidation steps was used to calculate the syngas yields according to **Figure 10**. Note that the reduced iron after reduction in the last cycle (cycle #7) was not re-oxidized, as it was kept for analyzing its phase composition via XRD. Therefore, no syngas yield during oxidation at cycle #7 was presented.

During reduction step (Figure 10a), as expected a large amount of CO_2 was observed during the first reduction (1.00 mmol/$g_{Fe_2O_3}$) arising from Fe_2O_3 reduction to Fe_3O_4 (0.059 mole of oxygen released, Figure 9), and total syngas yield decreased with cycles repetition (cycles #1-3). The syngas yields (especially H_2 and CO) grew with increasing reduction temperature (cycles #4-6), thereby confirming that the partial oxidation of CH_4 over iron oxide strongly depends on the reduction temperature, and temperatures higher than 1000 °C were required to favor reactions. However, a remarkable amount of H_2 associated with CH_4 cracking (3.01-5.57 mmol/$g_{Fe_2O_3}$) was inherently measured at cycles #5-6 because of higher reduction

temperatures (1100-1150 °C). Noticeably, CO_2 yield decreased with cycles repetition (except in cycle #5 at which the amount of CO_2 was higher than that obtained from cycle #1 as a result of the exacerbated temperature effect at 1150 °C), and it was not observed during the last cycle (cycle #7). This is because a large amount of the oxygen contained in the iron oxide lattice structure was released during the previous cycles favoring CO_2 formation. In fact, Fe_3O_4 reduction takes place into two stages: first the reduction from Fe_3O_4 to FeO (Equation 4) and then FeO to Fe (Equation 5). The first stage is faster than the second one presumably as a result of produced H_2 that reacts with Fe_3O_4 (Figure 2) but not with FeO.[27] The slower second reaction stage is caused by the material surface reduction resulting from sintering.[27] These variations may explain the decrease of CO_2 with cycles repetition (as evidenced in cycles #1-7) since the iron oxide structure does not completely return to the initial state despite passing the oxidation step (as proved by $n_{O,ox}$ values always lower than $n_{O,red}$, Figure 9), thereby leading to lower available oxygen for the subsequent reduction reaction.

During oxidation step (Figure 10b), most of the produced syngas yield at cycles #1-4 was ascribed to the production of H_2 formed by Equation 9. The CO ($C+H_2O$), CO_2 ($C+2H_2O$), H_2 ($C+H_2O$), and H_2 ($C+2H_2O$) yields formed by side reactions (Equation 10 and 11) were negligible, implying negligible amount of carbon deposition. In contrast, they were found in significant amounts in cycles #5-6, suggesting important impact of carbon deposition on syngas yields at 1100-1150 °C. Likewise, the reduced iron oxide composition after reduction in cycle #7 was characterized by XRD. Its phase identification is presented in **Figure S8**. The material is mainly composed of Fe, followed by traces of FeO, in agreement with the hard structure of iron in **Figure S9b**. Most of the iron oxide foam was converted to metallic Fe. It can be assumed that the iron oxide porous foam structure might be lastingly converted to metallic iron coarsened structure after being reduced at 1150 °C (cycle #5), and that the process is not reversible due to extremely high sintering entailing low re-oxidation ability, as observed in Figure S9b. This assumption can be evidenced by a sharp drop of H_2 ($Fe+H_2O$)

yield associated with the oxidation reaction in cycles #5-6 (ranging between 0.80-0.92 mmol/$g_{Fe_2O_3}$, Figure 10b) with extremely low oxygen uptake (0.013 mole for cycle #5 and 0.011 mole for cycle #6, Figure 9).

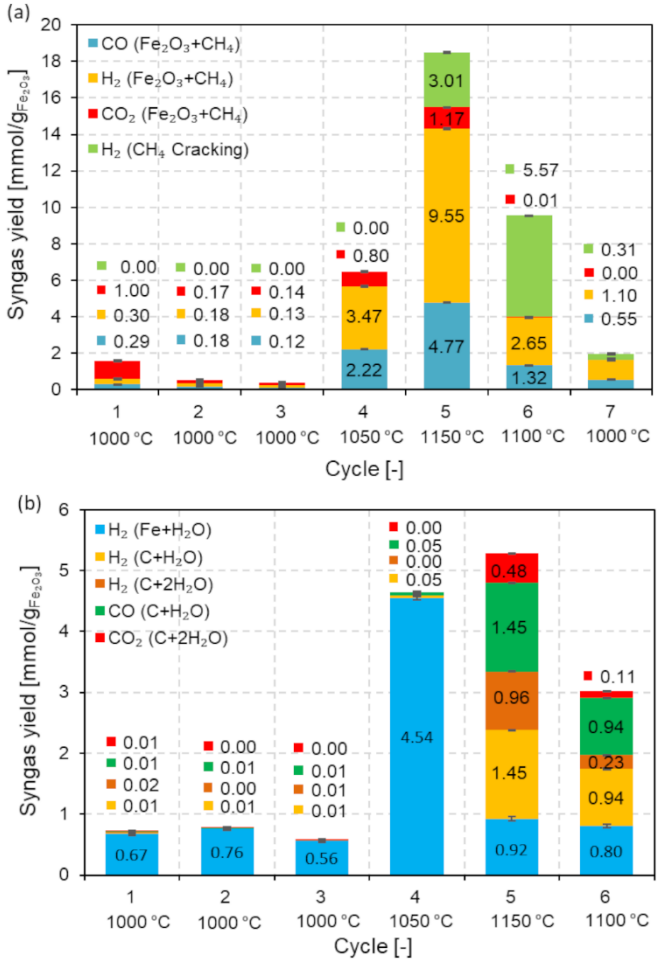

Figure 10. Syngas yields for (a) iron oxide reticulated porous foam reduction with CH_4 and (b) oxidation with H_2O cycled isothermally at temperatures in the range 1000-1150 °C.

In conclusion, the CLRM over both iron oxide powder and foam dramatically suffers from morphological instability (high sintering), slow reaction kinetics, and unfavorable oxidation because of strong material coarsening and densification, thus strongly altering the oxygen exchange reversibility. Then, the oxygen uptake during oxidation is always lower than the oxygen released during reduction because of low material thermal stability. For these reasons,

iron oxide is not suitable for CLRM process and would require stabilization for high-temperature processing (e.g. using inert ceramic support for improving material stability). Alternatively, iron oxide reduction using CH_4 is suitable for producing both metallic iron and syngas in a solar metallurgical process.

4.2. Methane reforming over cerium oxide

In order to compare the performance of oxygen carrier materials for CLRM, nonstoichiometric ceria was experimentally investigated. Pure ceria powder (total mass: 17.01 g, Figure S3c) was employed during six consecutive cycles at a constant temperature of 1000 °C. The same CH_4/Ar and H_2O/Ar gas mixtures were alternately delivered to carry out the reduction and oxidation reactions (CH_4: 0.2 Nl/min, H_2O: 200 mg/min, and Ar: 0.2 Nl/min).

Figure 11 shows syngas yields quantified from the integration of the measured syngas production rates for six reduction and oxidation cycles. According to Figure 11a, the H_2 (CeO_2+CH_4), CO, and CO_2 yields remained quite constant over the entire cycling (in the range 3.39-3.55 mmol/g_{CeO2} for H_2, 1.69-1.77 mmol/g_{CeO2} for CO, and 0.05 mmol/g_{CeO2} for CO_2). The total syngas yield was thus stable (in the range 5.77- 6.53 mmol/g_{CeO2}), in turn leading to stable patterns in δ_{red} (0.32-0.36), X_{CH_4} (40.8-44.3%, **Figure 12**), and selectivity (97.1-97.5% for H_2 and 98.5-98.6% for CO, Table S1) and demonstrating ceria cycling stability. The H_2 (CH_4 cracking) yield fluctuated slightly in the range 0.64-1.16 mmol/g_{CeO2} because of variation in the required CH_4 injection duration to reach ceria reduction completion in each cycle. This points out that increasing CH_4 injection duration favors the H_2 yield associated with CH_4 cracking.

Similarly, a stable pattern in the H_2 ($CeO_{2-\delta}$+H_2O) yield, produced during ceria oxidation (Equation 13) was observed (1.94-2.05 mmol/g_{CeO2}, Figure 11b). The amounts of gases produced by steam gasification of carbon deposition were fairly constant (in the range 0.08-

0.22 mmol/g_{CeO_2} for $H_2(C+H_2O)$, 0.11-0.22 mmol/g_{CeO2} for $H_2(C+2H_2O)$, 0.08-0.22 mmol/g_{CeO_2} for $CO(C+H_2O)$, and 0.06-0.11 mmol/g_{CeO_2} for $CO_2(C+2H_2O)$). Moreover, the δ_{ox} values were in the range 0.33-0.35, thus matching well the δ_{red} values (Figure 12) and demonstrating complete reduced ceria re-oxidation during cycling. These results thus confirmed the performance stability of ceria for solar CLRM.

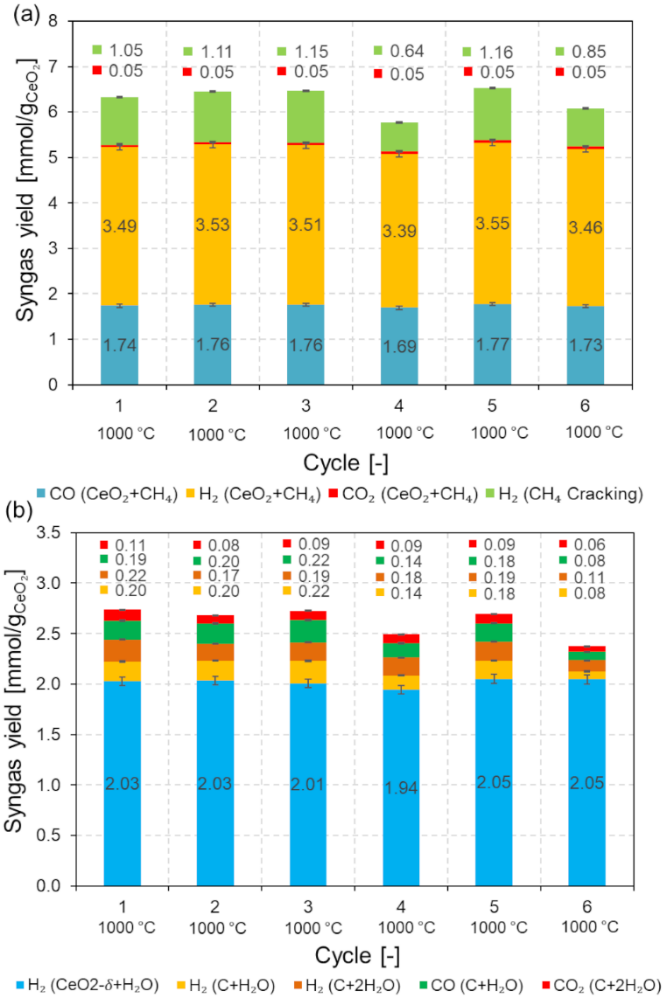

Figure 11. Syngas yields for both reduction and re-oxidation of ceria powder during 6 consecutive redox cycles at 1000 °C.

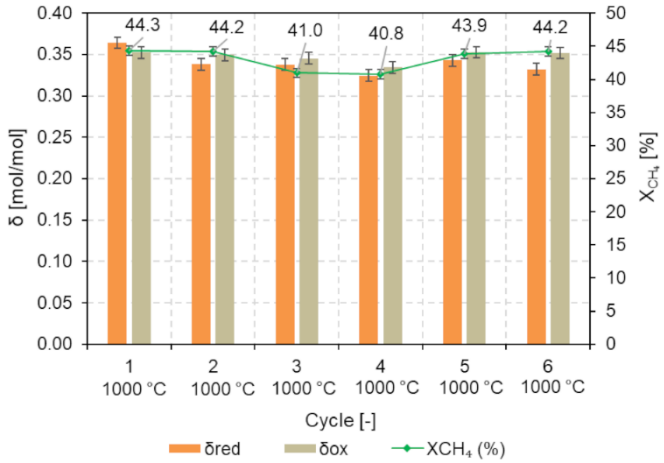

Figure 12. Comparison of δ_{red} and δ_{ox} in ceria powder along with CH_4 conversion during 6 consecutive redox cycles performed at 1000 °C.

In order to confirm the experimental repeatability and assess the effect of material shaping, a ceria reticulated porous foam (total mass: 18.37 g, Figure S3d) was prepared and then employed for solar CLRM. Experiments were carried out with 12 successive cycles at 950 °C (1 cycle), 1000 °C (10 cycles) and 1050 °C (1 cycle). The reacting and carrier gas flow rates were unchanged (0.2 Nl/min for CH_4, 200 mg/min for H_2O, and 0.2 Nl/min for Ar).

As expected, stable patterns in the H_2 (CeO_2+CH_4), CO, and CO_2 yields over 10 cycles at 1000 °C were evidenced, in the ranges 3.48-3.64 mmol/g_{CeO_2} for H_2 (CeO_2+CH_4), 1.74-1.82 mmol/g_{CeO_2} for CO, and 0.07-0.10 mmol/g_{CeO_2} for CO_2 (**Figure 13a**), thereby resulting in stable total syngas yield (5.67-6.80 mmol/g_{CeO_2}), δ_{red} (0.35-0.38) and X_{CH_4} evolution profile (46.9-60.9%, **Figure 14**) as well as constant selectivity (96.5-98.2% for H_2 and 95.1-98.1% for CO, Table S1). The H_2 (CH_4 cracking) yield at 1000 °C fluctuated slightly (in the range 0.35-1.27 mmol/g_{CeO_2}) because of a small difference in the CH_4 injection duration, as mentioned before. When either increasing or decreasing the temperature (1050 °C at cycle #5 or 950 °C at cycle #6), the total syngas yield varied significantly because of a change in the reaction kinetics. The maximum total syngas yield (7.48 mmol/g_{CeO_2}) was consequently found at the maximum temperature (1050 °C), demonstrating kinetic rate improvement (**Figure 15**).

Moreover, the H_2 (CH_4 cracking) yield was negligible at 900 °C, in agreement with the lowest X_{CH4} (20%); in contrast, it was maximal (2.0 mmol/g_{CeO_2}) at the highest temperature (1050 °C) in agreement with the highest X_{CH_4} (65.9%), thereby indicating that the extent of CH_4 cracking reaction is strongly dependent on the temperature.[9] For these reasons, a temperature trade-off at 1000 °C is advocated to hasten the kinetic rate of ceria reduction while alleviating the side reaction associated with CH_4 cracking.

In order to examine the reaction kinetics for ceria during methane-induced reduction, the Arrhenius expression was applied to evaluate the effect of temperature on ceria reduction rates.

$$k = A \cdot \exp(-E_a/RT) \quad (22)$$

Where *k* is the reaction rate constant, *A* is the pre-exponential factor, E_a is the activation energy, *R* is the gas constant and *T* is absolute temperature.

The reaction rate constants (k) were quantified from the peak production rates of H_2 and CO at 950 °C (cycle #6), 1000 °C (cycle #4), and 1050 °C (cycle #5). The logarithm evolution of the reaction rates versus inverse temperature (Equation 22) was subsequently plotted (**Figure 15**) to determine the activation energy (E_a) of the ceria reduction process. As a result, the slope of ln k for both H_2 and CO production rates increased linearly with the inverse temperature. The E_a values were 114.2 kJ/mol for H_2 and 93.4 kJ/mol for CO. The E_a value related to H_2 production rates was slightly higher compared to that of CO as a result of the side reaction effect attributed to CH_4 cracking. This side reaction produces additional H_2 and thus modifies the global H_2 production rate arising only from the reaction with ceria. In contrast, CO is only produced from methane reforming (Equation 12) and better represents the kinetics of ceria reduction reaction. In addition, the E_a for reduction was consistent with previous study [30].

Regarding oxidation (Figure 13b), the H_2 ($CeO_{2-\delta}+H_2O$) yield was stable at 1000 °C (in the range 2.04-2.17 mmol/g_{CeO_2}), except for cycles #5 and #6 caused by the temperature impact during the reduction step. Likewise, the $H_2(C+H_2O)$, $H_2(C+2H_2O)$, $CO(C+H_2O)$, and $CO_2(C+H_2O)$ yields at 1000 °C were fairly constant in negligible amounts (0.11-0.18, 0.04-0.10, 0.11-0.18, and 0.02-0.05 mmol/g_{CeO_2}, respectively). The total syngas yield was in the range 2.38-2.57 mmol/g_{CeO_2}, and δ_{ox} was in the range 0.35-0.37 (consistent with δ_{red}) (Figure 14). Thus, the cycling stability of ceria was validated with respect to stable patterns in produced syngas, δ, and X_{CH_4}, thereby outperforming iron oxide (whether in the form of powder or foam structures) and exhibiting superior thermochemical stability over cycles.

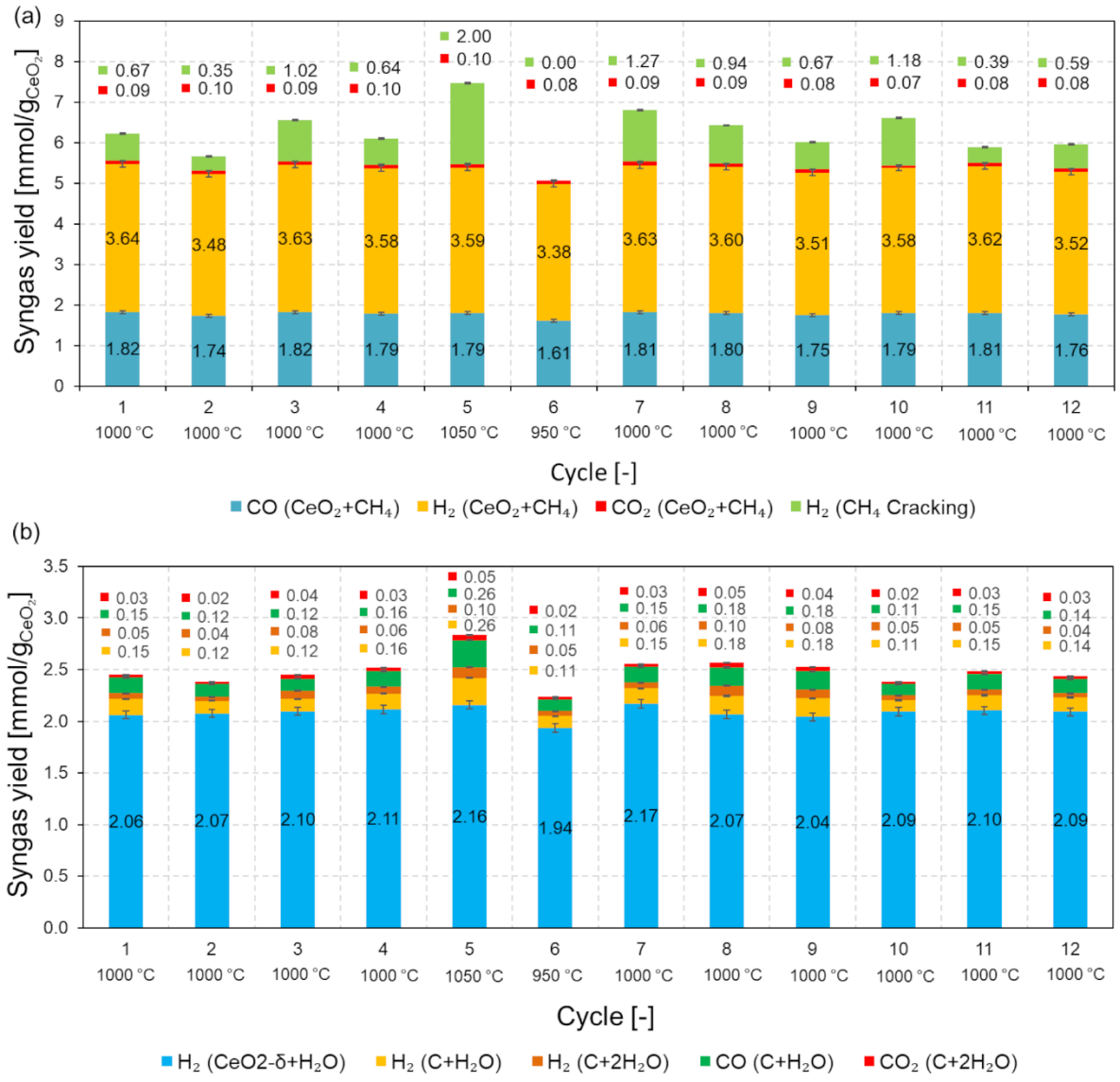

Figure 13. Syngas yields for both reduction and re-oxidation of ceria porous foam during 12 consecutive redox cycles performed isothermally.

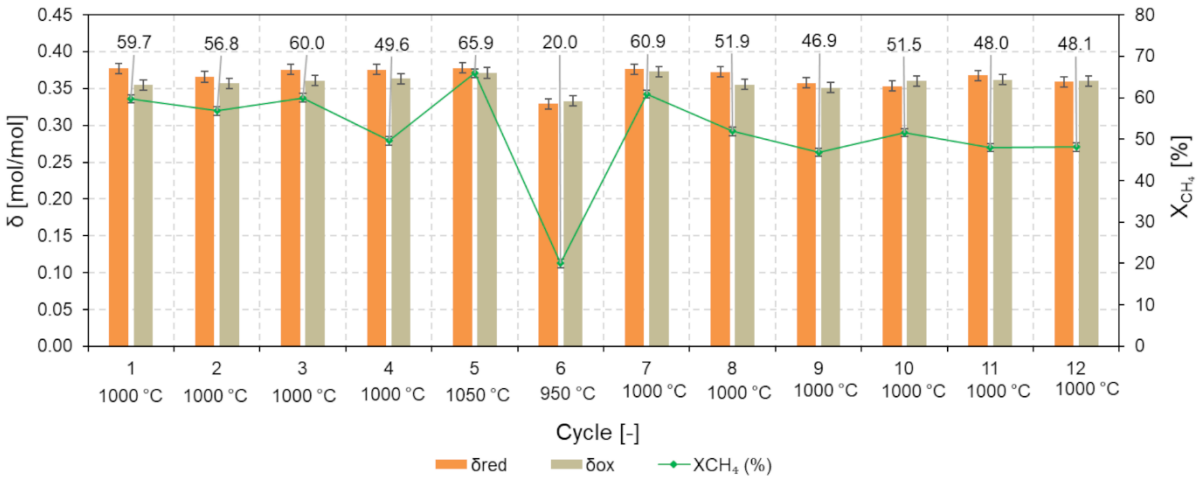

Figure 14. Comparison of δ_{red} and δ_{ox} in ceria foam along with CH_4 conversion during 12 consecutive redox cycles performed isothermally.

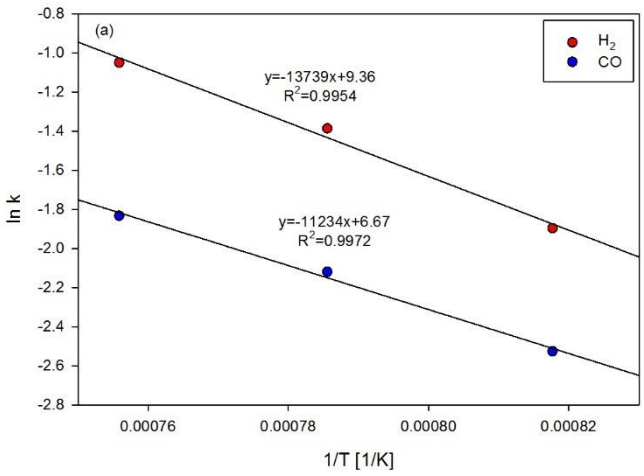

Figure 15. Arrhenius plot for H_2 and CO production rates in the range 950-1050 °C during ceria foam reduction.

The main advantages of CeO_2 when compared with iron oxide have thus been highlighted, including faster reaction rates, reversibility and cycling stability. Besides, combining both

cerium and iron oxides may promote the oxygen carrier performance by taking advantage of their mutual benefits, while alleviating the drawbacks of both iron oxide (sintering and poor reaction reversibility) and cerium oxide (higher cost and moderate oxygen exchange capacity).

5. Conclusion

Solar chemical looping reforming of methane (CLRM) combined with isothermal H_2O splitting over iron and cerium oxides was thermodynamically and experimentally investigated in a directly-irradiated lab-scale solar reactor using concentrated solar heat for supplying process energy. The thermodynamic analysis provided insights into the theoretically possible chemical reactions and equilibrium species distribution for comparison with experimental results.

Iron oxide (Fe_2O_3) in the form of powder or porous foam showed relatively low reaction rate when reacting with methane at 1000 °C, and the reduction extent strongly depended on temperature. However, increasing the temperature (≥1100 °C) resulted in strong sintering (dense structure), lowered syngas yield, and material deactivation. In contrast, cerium oxide (CeO_2) showed faster reaction rates than iron oxide when reacting with methane at 1000 °C, and increasing the temperature between 900-1050 °C promoted syngas yield and ceria reduction kinetics (with activation energy for ceria foam reduction in the range 93.4-114.2 kJ/mol). Stable patterns in the ceria reduction and oxidation extents, CH_4 conversion, and syngas yields during successive cycles for both powder and reticulated porous foam demonstrated remarkable thermochemical cycling stability.

Thus, utilizing iron oxide (Fe_2O_3) as oxygen carrier is not suitable for solar CLRM with respect to poor material re-oxidation capability; instead, iron oxide reduction with CH_4 could be an attractive route for producing both metallic iron and syngas via CO_2-free solar metallurgical process. For these reasons, the use of cerium oxide as oxygen carrier for solar CLRM is more appropriate than iron oxide. The advantages of using ceria as oxygen carrier

have thus been demonstrated, such as faster reaction rates and superior thermochemical cycling stability (oxygen can be released and recovered reversibly in the oxide crystal lattice), which are key assets for the two-step solar chemical-looping process. Combining concentrated solar energy and CLRM was shown to be a promising and sustainable pathway toward clean solar fuels. Further work should be focused on taking the benefits of both iron and cerium oxides by considering their mixed oxides to promote the oxygen carrier performance.

Supporting Information
Supporting Information is available from the Wiley Online Library or from the author.

Acknowledgements
The King Mongkut's Institute of Technology Ladkrabang (KMITL), Thailand and the Franco-Thai scholarship program are gratefully acknowledged for fellowship granting.

Received: ((will be filled in by the editorial staff))
Revised: ((will be filled in by the editorial staff))
Published online: ((will be filled in by the editorial staff))

References

[1] Q. Zheng, C. Janke, R. Farrauto, *Appl. Catal. B Environ*. **2014**, 160–161, 525–533.

[2] Q. Song, R. Xiao, Y. Li, L. Shen, *Ind. Eng. Chem. Res.* **2008**, *47*, 4349–4357.

[3] G. Zhang, Y. Dong, M. Feng, Y. Zhang, W. Zhao, H. Cao, *Chem. Eng. J.* **2010**, *156*, 519–523.

[4] G. Zhang, A. Su, Y. Du, J. Qu, Y. Xu, *J. Colloid Interface Sci*. **2014**, *433*, 149–155.

[5] G. Zhang, Y. Du, Y. Xu, Y. Zhang, *J. Ind. Eng. Chem.* **2014**, 20, 1677–1683.

[6] K. J. Warren, J. Reim, K. Randhir, B. Greek, R. Carrillo, D. W. Hahn, J. R. Scheffe, *Energy Technol.* **2017**, *5*, 2138–2149.

[7] S. Chuayboon, S. Abanades, S. Rodat, *Chem. Eng. J*. **2019**, *356*, 756–770.

[8] P.T. Krenzke, J.R. Fosheim, J. Zheng, J.H. Davidson, *Int. J. Hydrogen Energy* **2016**, *41*, 12799–12811.

[9] J. R. Fosheim, B. J. Hathaway, J. H. Davidson, *Energy* **2019**, *169*, 597–612.

[10] C. Wieckert, A. Steinfeld, *J. Sol. Energy Eng*. **2001**, *124*, 55–62.

[11] T. Kodama, T. Shimizu, A. Aoki, Y. Kitayama, *Energy & Fuels* **1997**, *11*, 1257–1263.

[12] H. I. Villafan-Vidales, S. Abanades, M. Montiel-Gonzalez, H. Romero, *Energy Technol* **2016**, *5*, 692–702.

[13] M. Welte, K. Warren, J. R. Scheffe, A. Steinfeld, *Ind. Eng. Chem. Res.* **2017**, *56*, 10300–10308.

[14] S. Abanades, P. Charvin, G. Flamant, P. Neveu, *Energy* **2006**, *31*, 2805–22.

[15] A. Steinfeld, A. Frei, P. Kuhn, D. Wuillemin, *Int. J. Hydrogen Energy* **1995**, *20*, 793–804.

[16] M. E. Gálvez, A. Frei, G. Albisetti, G. Lunardi, A. Steinfeld, *Int. J. Hydrogen Energy* **2008**, *33*, 2880–2890.

[17] K. Otsuka, M. Hatano, A. Morikawa, *J. Catal.* **1983**, *79*, 493–496.

[18] K. Otsuka, T. Ushiyama, I. Yamanaka, *Chem. Lett.* **1993**, *22*, 1517–1520.

[19] K. Li, H. Wang, Y. Wei, D. Yan, *Appl. Catal. B Environ.* **2010**, *97*, 361–372.

[20] K. Li, H. Wang, Y. Wei, D. Yan, *Chem. Eng. J.* **2010**, *156*, 512–518.

[21] K. Otsuka, Y. Wang, M. Nakamura, *Appl. Catal. A Gen.* **1999**, *183*, 317–324.

[22] C. L. Muhich, S. Blaser, M. C. Hoes, A. Steinfeld, *Int. J. Hydrogen Energy* **2018**, *43*, 18814–18831.

[23] J. T. Jang, K. J. Yoon, G. Y. Han, *Sol. Energy* **2014**, *101*, 29–39.

[24] H. H. Jeong, J. H. Kwak, G. Y. Han, K. J. Yoon, *Int. J. Hydrogen Energy* **2011**, *36*, 15221–15230.

[25] T, Shimizu, Y, Kitayama, T, Kodama, *Energy & Fuels* **2001**, *15*, 463–469.

[26] L. Wang, T. Ma, Z. Chang, H. Li, M. Fu, X. Li, *Sol. Energy* **2019**, *177*, 772–781.

[27] A. Steinfeld, P. Kuhn, J. Karni, *Energy* **1993**, *18*, 239–249.

[28] K. S. Kang, C. H. Kim, K. K. Bae, W. C. Cho, S. H. Kim, C. S. Park, *Int. J. Hydrogen Energy* **2010**, *35*, 12246–12254.

[29] P. Furler, J. Scheffe, D. Marxer, M. Gorbar, A. Bonk, U. Vogt, *Phys. Chem. Chem. Phys.* **2014**, *16*, 10503–10511.

[30] M. M. Nair, S. Abanades, *Energy & Fuels* **2016**, *30*, 6050–6058.

[31] O. T. Sørensen, *J. Solid State Chem.* **1976**, *18*, 217–233.

[32] A. C. Gladen, J. H. Davidson, *Sol. Energy* **2016**, *139*, 524–532.

[33] C. Lu, K. Li, H. Wang, X. Zhu, Y. Wei, M. Zheng, *Appl. Energy* **2018**, *211*, 1–14.

[34] M. F. Bleeker, H. J. Veringa, S. R. A. Kersten, *Appl. Catal. A Gen.* **2009**, *357*, 5–17.

[35] S. Abanades, G. Flamant, *Sol. Energy* **2006**, *80*, 1611–1623.

[36] X. Zhu, H. Wang, Y. Wei, K. Li, X. Cheng, *J. Nat. Gas Chem.* **2011**, *20*, 281–286.

[37] P. T. Krenzke, J. H. Davidson, *Energy & Fuels* **2014**, *28*, 4088–4095.

[38] X. Zhu, K. Li, Y. Wei, *Energy & Fuels* **2014**, *28*, 754–760.

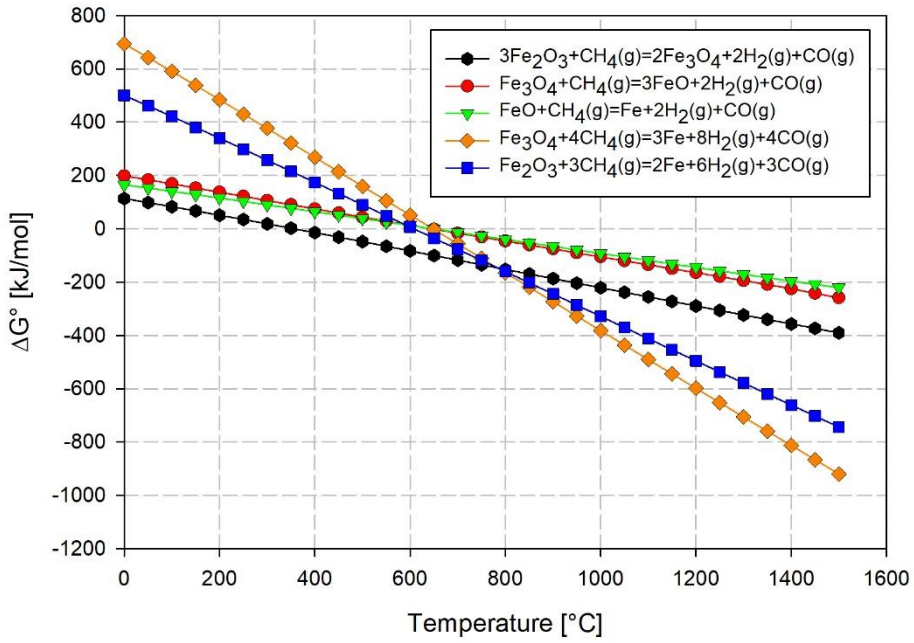

Figure 1. ΔG° variations for iron oxides reduction with methane as a function of temperature.

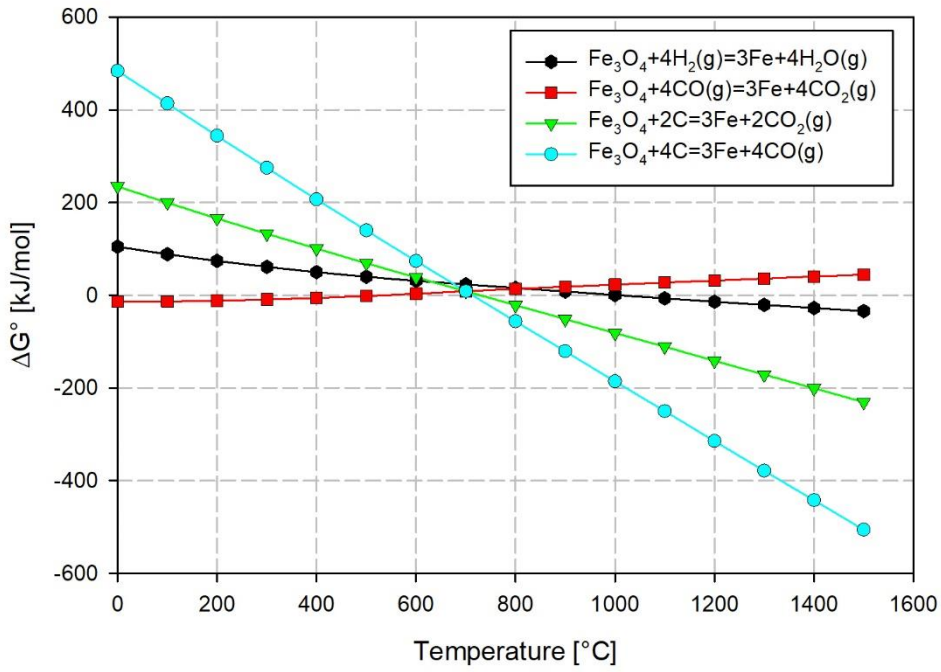

Figure 2. ΔG° variations for the reactions of Fe_3O_4 with H_2, CO, and C as a function of temperature.

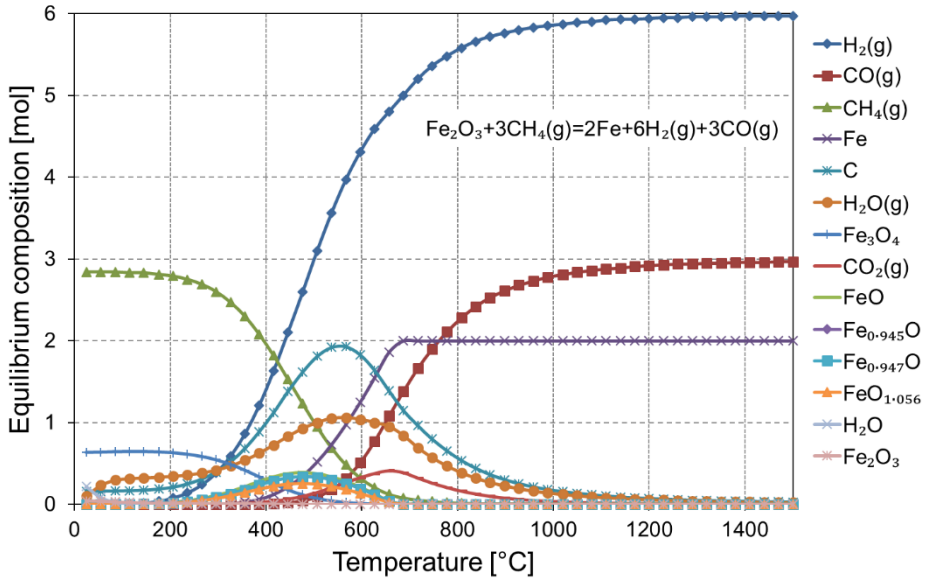

Figure 3. Thermodynamic equilibrium composition of methane reforming over Fe_2O_3 as a function of temperature at 1 bar.

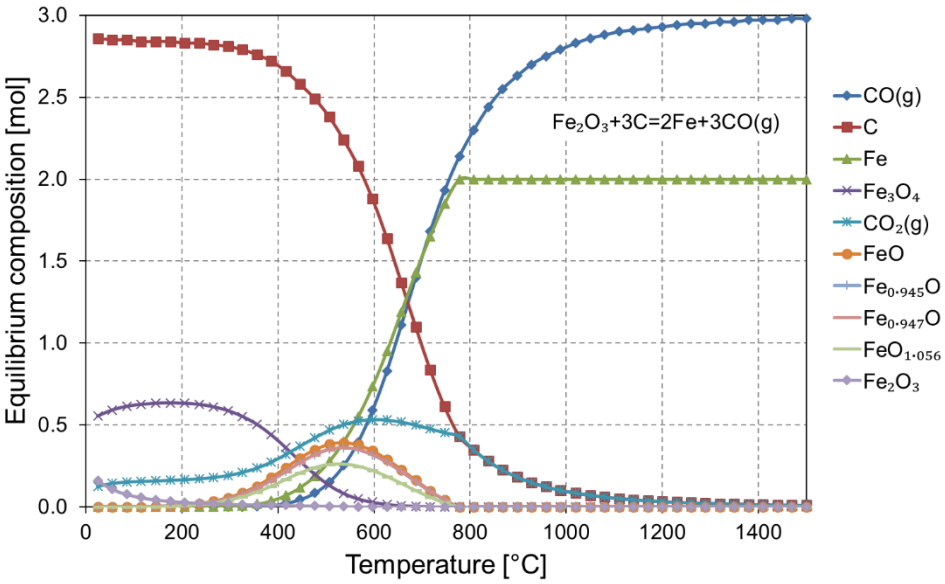

Figure 4. Thermodynamic equilibrium composition of Fe_2O_3 carbothermal reduction as a function of temperature at 1 bar.

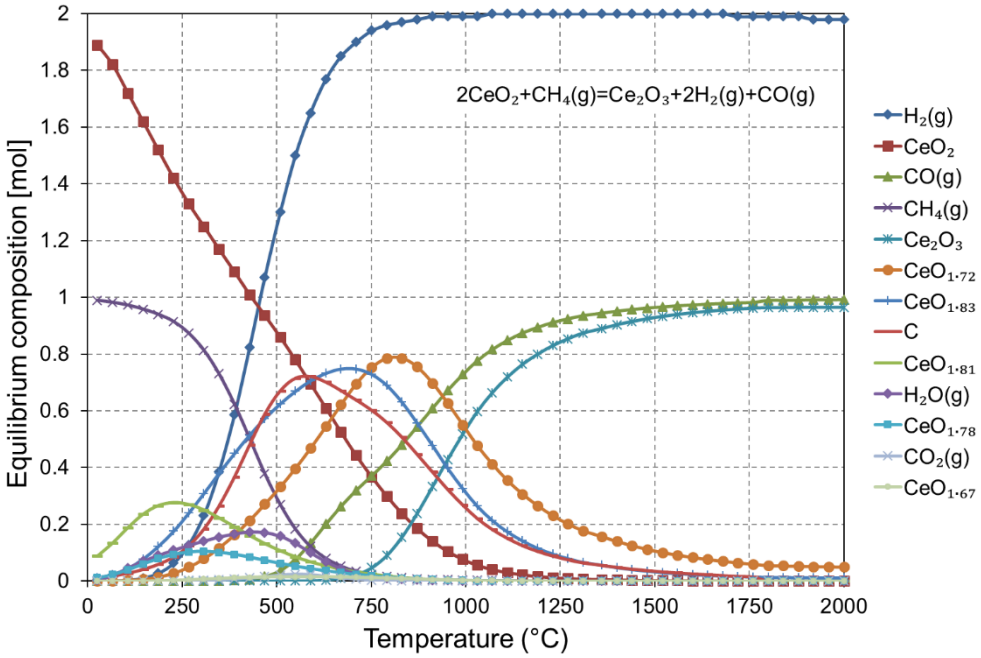

Figure 5. Thermodynamic equilibrium composition of methane reforming over ceria as a function of temperature at 1 bar.

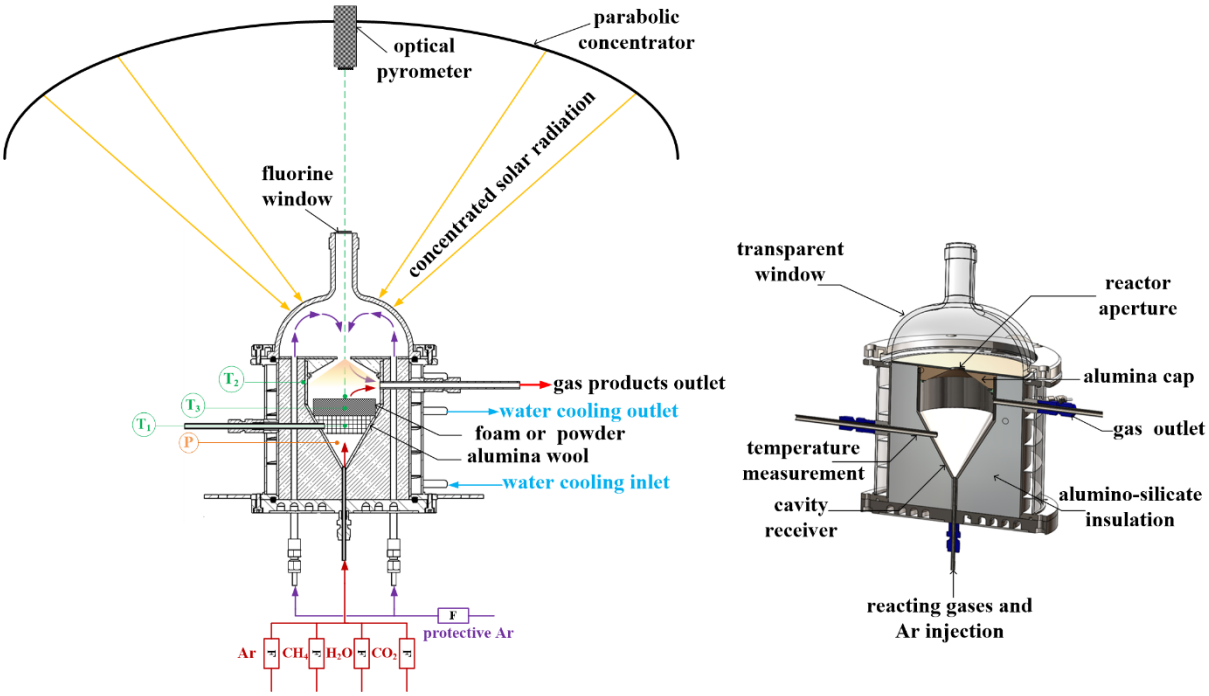

Figure 6. Schematic of the 1.5 kW_{th} directly-irradiated solar reactor and external components (left) and 3D cross section of the solar reactor (right).

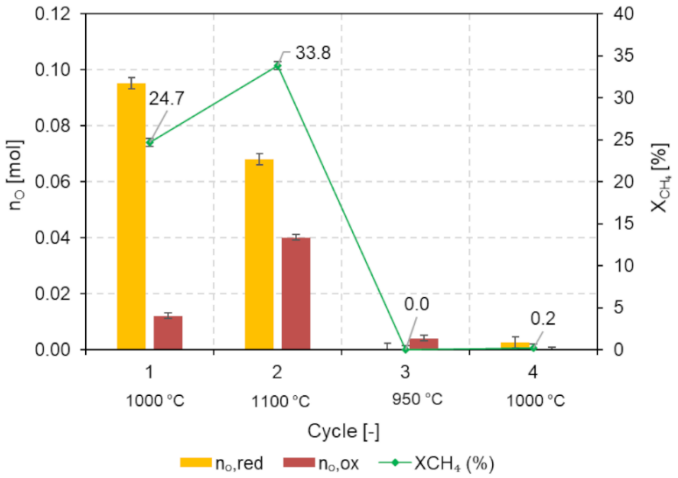

Figure 7. Comparison of $n_{O,red}$ and $n_{O,ox}$ along with CH_4 conversion during four consecutive redox cycles with iron oxide powder performed at 950-1100 °C.

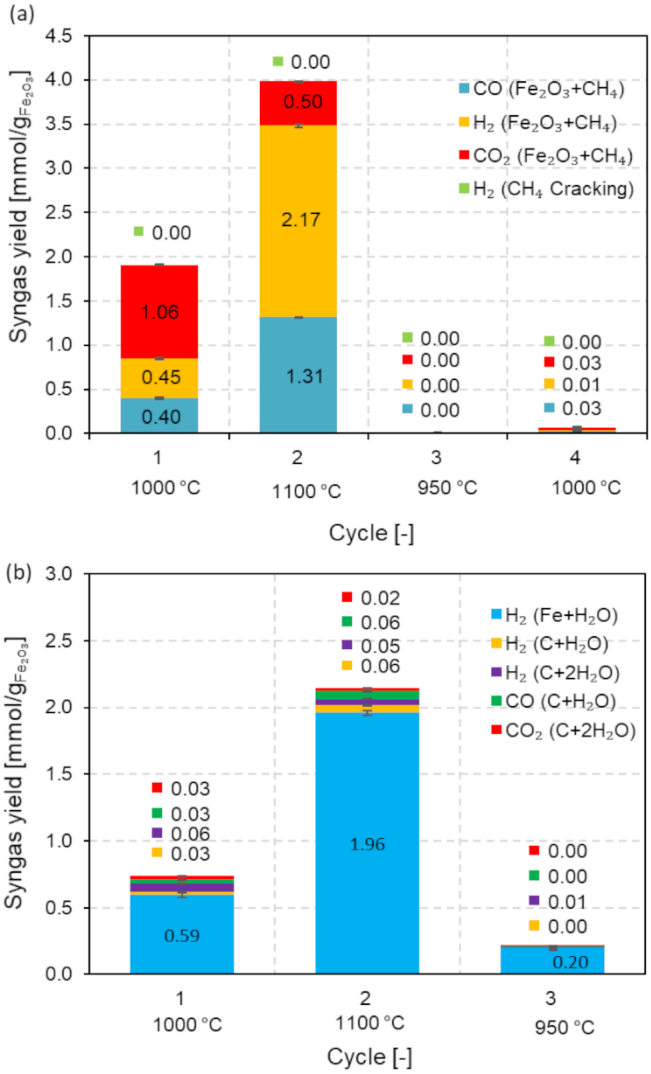

Figure 8. Syngas yields for (a) iron oxide powder reduction with CH_4 and (b) oxidation with H_2O during isothermal cycles at temperatures in the range 950-1100 °C.

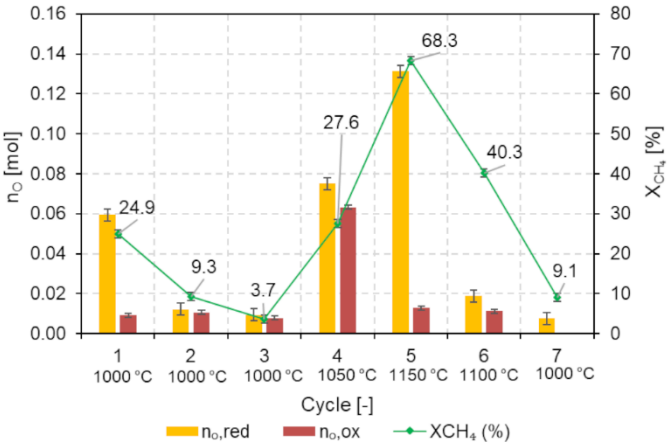

Figure 9. Comparison of $n_{O,red}$ and $n_{O,ox}$ along with CH_4 conversion during seven consecutive redox cycles with iron oxide foam performed at 1000-1150 °C.

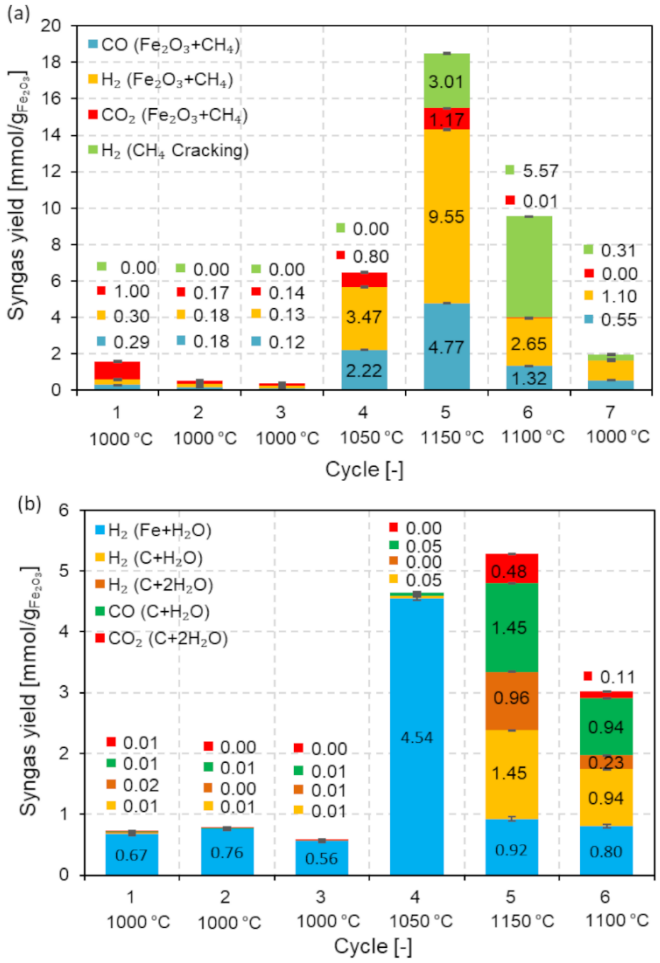

Figure 10. Syngas yields for (a) iron oxide reticulated porous foam reduction with CH_4 and (b) oxidation with H_2O cycled isothermally at temperatures in the range 1000-1150 °C.

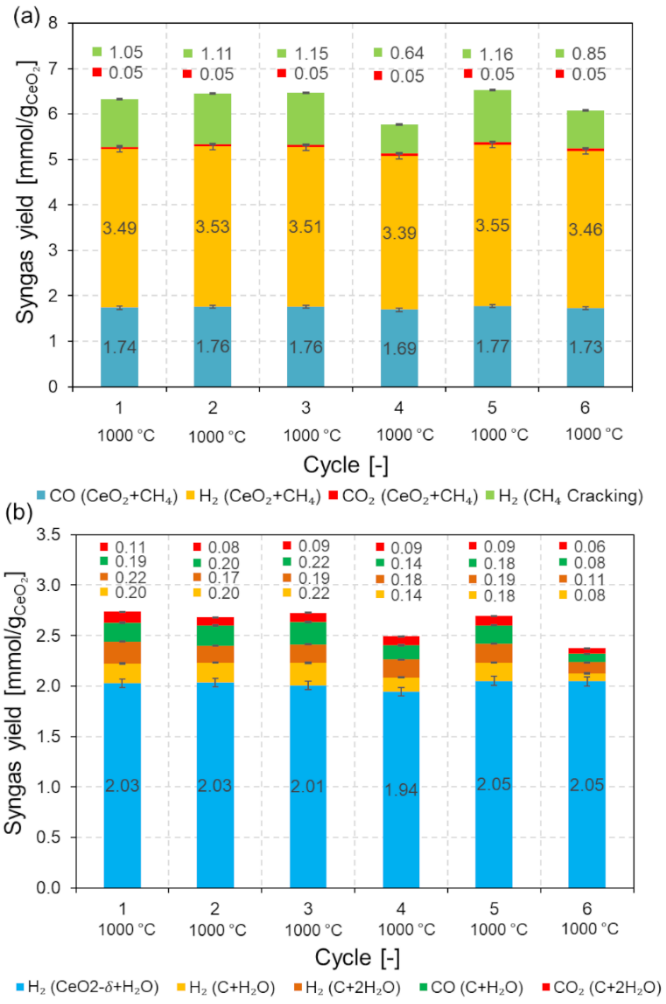

Figure 11. Syngas yields for both reduction and re-oxidation of ceria powder during 6 consecutive redox cycles at 1000 °C.

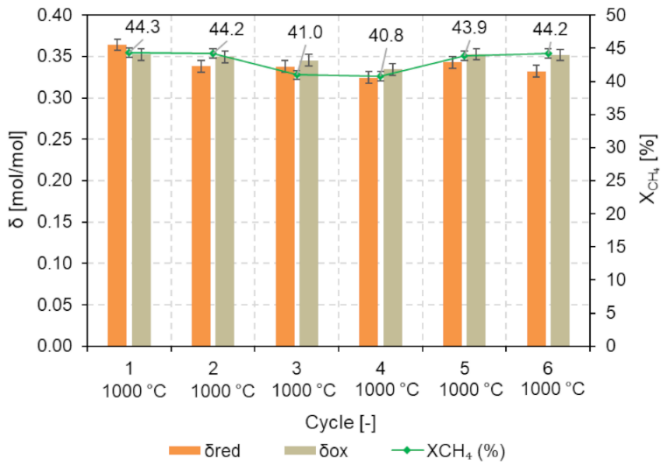

Figure 12. Comparison of δ_{red} and δ_{ox} in ceria powder along with CH_4 conversion during 6 consecutive redox cycles performed at 1000 °C.

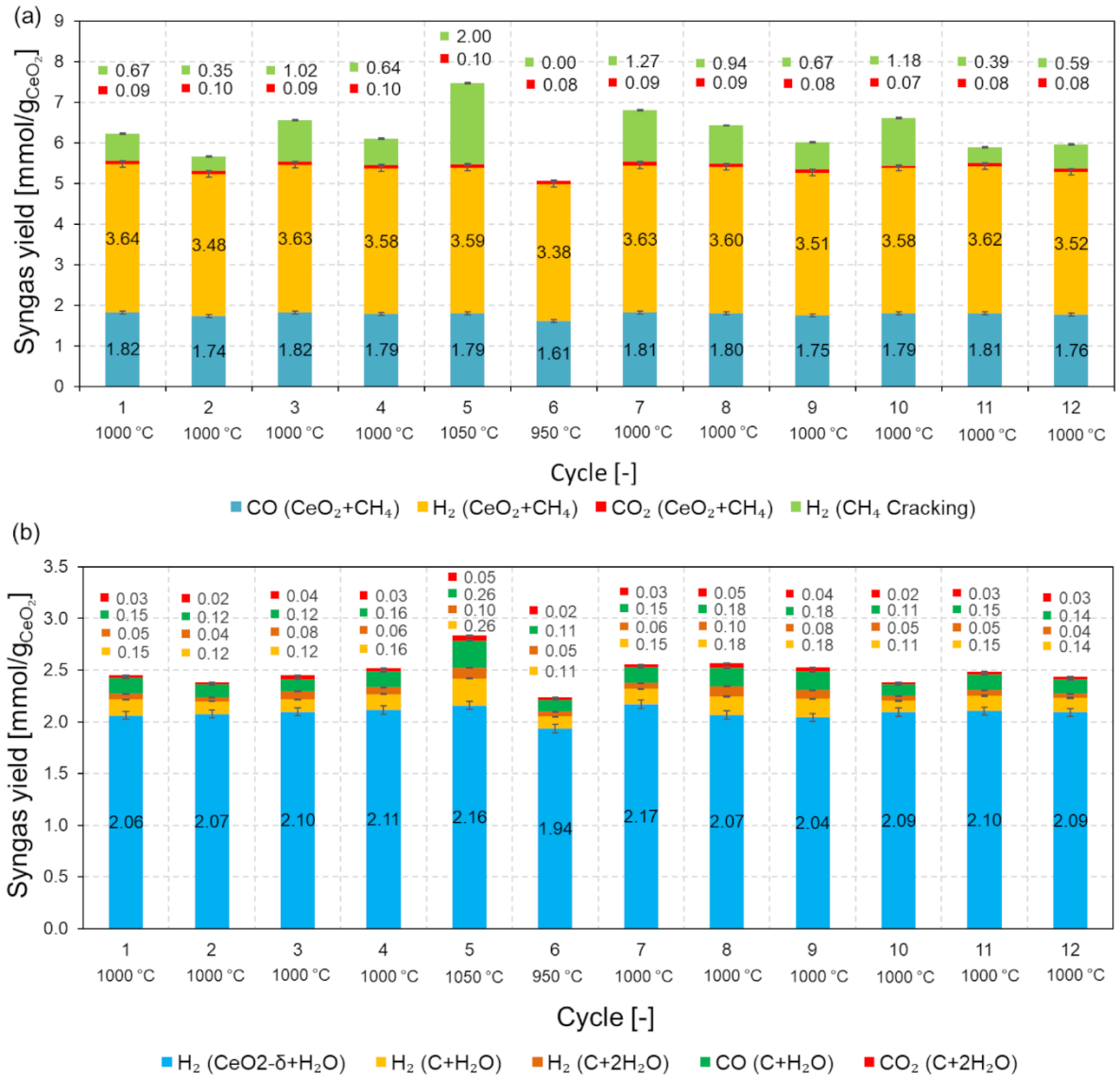

Figure 13. Syngas yields for both reduction and re-oxidation of ceria porous foam during 12 consecutive redox cycles performed isothermally.

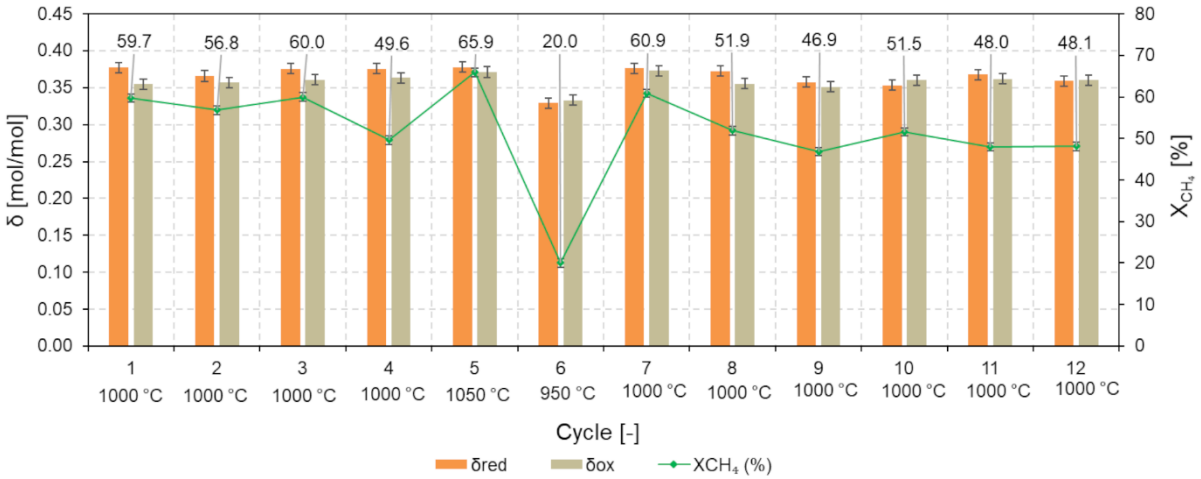

Figure 14. Comparison of δ_{red} and δ_{ox} in ceria foam along with CH_4 conversion during 12 consecutive redox cycles performed isothermally.

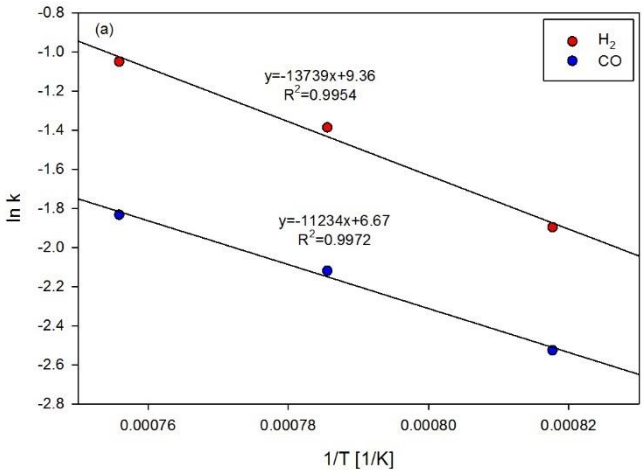

Figure 15. Arrhenius plot for H_2 and CO production rates in the range 950-1050 °C during ceria foam reduction.

Syngas is produced in a solar chemical reactor using reversible cycling of solid oxides for isothermal alternating methane reforming and H_2O splitting. Solar chemical looping reforming using oxygen carrier materials promotes methane valorization and offers an efficient means of storing intermittent solar energy into renewable clean fuels.

Solar fuels

S. Chuayboon, S. Abanades*, S. Rodat

Stepwise solar methane reforming and water-splitting via lattice oxygen transfer in iron and cerium oxides